

EXPERIMENTAL AND MODELING STUDY OF MICRO-PUMP DIRECT CURRENT  
MOTORS FOR PORTABLE DIRECT METHANOL FUEL CELL APPLICATIONS

By

ANUPAM VILAS PATIL

A THESIS PRESENTED TO THE GRADUATE SCHOOL  
OF THE UNIVERSITY OF FLORIDA IN PARTIAL FULFILLMENT  
OF THE REQUIREMENTS FOR THE DEGREE OF  
MASTER OF SCIENCE

UNIVERSITY OF FLORIDA

2011

© 2011 Anupam Vilas Patil

To my parents, Mrs. Vasudha and Dr. Vilas Patil; and my sister Abhilasha Patil-Tandel  
This work would not have been possible without your love and support  
You have inspired me to become who I am today  
I dedicate this work to you

## ACKNOWLEDGMENTS

The completion of this work was possible only because of immense contribution from Dr. William Lear. I am extremely grateful to Dr. William Lear and Dr. James Fletcher for encouraging, advising and supporting me right from my first day of the masters program. I am also grateful to Dr. Oscar Crisalle for his guidance throughout the project. I would also like to thank Dr. Herbert Ingley for serving on my committee.

I would like to thank the most important people in my life, my parents and my sister for their constant support and love. I am indebted to my colleagues at the University of Florida's Fuel Cell Research Laboratory for their invaluable guidance. Without assistance of Praneeth Pillarisetti, the experimentation portion of this work would not have been possible. Sydni Credle has always been a very patient mentor. Cheng-Chan Kuo has provided me with his incredible insights on several occasions. The professionalism of everyone in this research facility will continue to inspire me throughout my career. I would also like to thank my colleagues at the University of North Florida for their assistance on several occasions.

I also take this opportunity to thank my all my friends especially Aditya Karnik, Kshitij Padhye, Akshay Bharadwaj, Ashwini Khade, Asmita Chitale, Sumit Bhangdiya and Samiksha Shinde for being like a family. I would also like to thank my friends back home for their support. Last but not the least; I would like to thank God for giving me this opportunity. Nothing was possible without his love.

## TABLE OF CONTENTS

	<u>page</u>
ACKNOWLEDGMENTS.....	4
LIST OF TABLES.....	8
LIST OF FIGURES.....	9
ABSTRACT .....	11
CHAPTER	
1 INTRODUCTION .....	12
1.1 Overview .....	12
1.2 Recirculation Pump.....	14
1.3 Goals and Objectives.....	15
1.4 Thesis Organization .....	15
2 EXPERIMENTATION INVESTIGATION.....	17
2.1 Pump under Consideration .....	17
2.1.1 Market Research .....	17
2.1.2 Candidate Pump.....	17
2.2 General Purpose Micro Pump Test Rig .....	18
2.2.1 Experimental Apparatus .....	18
2.2.2 Hardware Components.....	21
2.2.3 Hardware for Data Acquisition and Control of Test Parameters .....	22
2.2.3.1 Differential pressure head across the pump .....	22
2.2.3.2 Pressure gauge calibration .....	23
2.2.3.3 Differential pressure gauge calibration curves .....	24
2.2.3.4 Upstream pressure .....	24
2.2.3.5 Flow rate .....	24
2.2.3.6 Flow meter calibration.....	25
2.2.3.7 Actuation voltage .....	25
2.2.3.8 Current to drive the pump .....	25
2.2.3.9 Motor speed.....	25
2.2.3.10 Data acquisition .....	26
2.2.4 Test Procedure .....	26
2.2.5 Data Reduction.....	27
2.3 D.C. Motor Test Setup .....	28
2.3.1 Hardware Components.....	29
2.3.1.1 Rotating assembly.....	29
2.3.1.2 Pendulum assembly.....	29
2.3.2 Hardware for Data Collection and Control of Test Parameters.....	30
2.3.2.1 Optical tachometer .....	30

2.3.2.2 Rotary encoder .....	30
2.3.2.3 Current shunt .....	30
2.3.2.4 Data acquisition .....	30
2.3.3 Test Procedure .....	30
2.3.4 Data Reduction.....	31
2.3.4.1 Angle of deflection of the pendulum .....	31
2.3.4.2 Torque.....	32
2.3.4.3 Motor speed .....	32
2.3.4.4 Input power .....	32
2.3.4.5 Output power .....	33
2.3.4.6 Efficiency.....	33
<b>3 EXPERIMENTAL RESULTS.....</b>	<b>34</b>
3.1 General Purpose Micro Pump Test Rig .....	34
3.2 D.C. Motor Test Rig .....	37
3.3 Experimental results for pump .....	40
<b>4 DIRECT CURRENT MOTOR MODEL.....</b>	<b>43</b>
4.1 Need for Finite Element Analysis.....	43
4.2 Finite Element Method Magnetics.....	44
4.3 Application of FEMM to DC Motor Model.....	44
4.3.1 Pre-processing.....	44
4.3.2 Boundary Conditions.....	47
4.3.3 Mesh Generation .....	49
4.3.4 Solution Scheme.....	50
4.4 DC Motor Model.....	51
4.4.1 Determination of Torque Constant .....	51
4.4.2 Determination of Voltage Constant.....	54
4.4.3 Motor Speed Calculation .....	57
4.4.4 Parameterization of Voltage Constant .....	57
4.4.5 Friction Model.....	58
4.4.6 FEM and DC Motor Model Results .....	59
<b>5 MODELING RESULTS .....</b>	<b>60</b>
5.1 FEM Results .....	60
5.2 Application of DC Motor Model to FEM Results.....	65
<b>6 CONCLUSIONS AND RECOMMENDATIONS FOR FUTURE WORK.....</b>	<b>69</b>
<b>APPENDIX</b>	
<b>A UNCERTAINTY ANALYSIS.....</b>	<b>72</b>
1.1 UF Pump Test Apparatus .....	72
1.1.1 Energizing Voltage for Pump-Motor Combination .....	72

1.1.2 Current .....	72
1.1.3 Flow Rate .....	72
1.1.4 Differential Pressure .....	72
1.1.5 Input Power .....	73
1.1.6 Output Power .....	73
1.1.7 Efficiency .....	73
1.2 Micro-Dynamometer .....	73
1.2.1 Voltage .....	73
1.2.2 Current .....	74
1.2.3 Angle of Deflection .....	74
1.2.4 Torque .....	74
1.2.5 Motor Speed .....	74
1.2.6 Input Power .....	74
1.2.7 Output Power .....	75
1.2.8 Efficiency .....	75
1.3 Inferred Results .....	75
<b>B MODEL GEOMETRY.....</b>	<b>76</b>
2.1 Motor Rotor.....	76
2.2 Motor Casing .....	77
2.3 Permanent Magnet .....	78
<b>LIST OF REFERENCES .....</b>	<b>79</b>
<b>BIOGRAPHICAL SKETCH.....</b>	<b>80</b>

## LIST OF TABLES

<u>Table</u>	<u>page</u>
4-1 Description of DC motor components .....	47
5-1 Comparison of experimental and analytical values of motor parameters .....	68

## LIST OF FIGURES

<u>Figure</u>	<u>page</u>
1-1 DMFC System Architecture.....	13
2-1 Micro-pump experimental facility layout. ....	19
2-2 General purpose pump test apparatus at University of Florida .....	20
2-3 Constant pressure head reservoir schematic.....	22
2-4 Test schematic for differential pressure gauge calibration .....	23
2-5 Motor Test Rig developed at University of North Florida.....	28
2-6 Micro-dynamometer in operation at the University of North Florida .....	29
2-7 Torque acting on a pendulum system comprising of magnet and counter weight...	32
3-1 Plot of flow rate of KNF pump as a function of differential pressure.....	35
3-2 Plot of efficiency and power consumption of KNF pump as a function of differential pressure at two actuation voltages.....	36
3-3 Plot of Torque as a function of rotational speed.....	38
3-4 Plot of Current and Efficiency as a function of rotational speed .....	39
3-5 Plot of torque versus current for the experimental data.....	40
3-6 Plot of pump efficiency as a function of differential pressure. ....	41
4-1 FEMM Model of permanent magnet brush type D.C. motor with graphic illustration .....	45
4-2 Commutator Brush arrangement for D.C. motor. ....	46
4-3 Comparison of the external boundary and the motor size .....	48
4-4 Triangular mesh in the motor geometry. ....	49
4-5 A closer view at space between rotor and magnet depicting a finer mesh compared to neighboring spaces.....	50
4-6 Schematic of DC motor coil. A) Single current coil in an external magnetic field. B) Side view of the current carrying coil in external magnetic field. ....	52
4-7 Schematic of a single coil rotating in an external magnetic field. ....	55

5-1 Magnetic flux densities at the reference orientation .....	61
5-2 Magnetic field intensities at the reference location.....	61
5-3 Magnetic field intensity at the air gap between magnet and rotor .....	62
5-4 Variation of torque with rotor angular position .....	63
5-5 Plot for electromagnetic torque and experimental torque versus current .....	64
5-6 Comparison of experimental and analytical electromagnetic torque values for 4V and 6V .....	65
5-7 Comparison of experimental and analytical load torque values for 4V and 6V .....	66
5-8 Comparison of experimental and analytical motor efficiency for 4V and 6V.....	67
Appendix 2-1 Laminated steel rotor in the DC Motor .....	76
Appendix 2-2 Steel casing in the DC motor.....	77
Appendix 2-3 Ceramic magnet in the DC motor.....	78

Abstract of Thesis Presented to the Graduate School  
of the University of Florida in Partial Fulfillment of the  
Requirements for the Degree of Master of Science

EXPERIMENTAL AND MODELING STUDY OF MICRO-PUMP DIRECT CURRENT  
MOTORS FOR PORTABLE DIRECT METHANOL FUEL CELL APPLICATIONS

By

Anupam Vilas Patil

August 2011

Chair: William Lear  
Cochair: Oscar Crisalle  
Major: Mechanical Engineering

A portable direct methanol fuel cell system is under investigation at the University of Florida Fuel Cell Research Laboratory. The anode recirculation pump-motor unit is a vital part of the system and is also among the highest parasitic loads. The losses can be split into pump fluid dynamic losses and motor electromagnetic and frictional losses.

An experimental apparatus was built to test micro-pumps. One of the commercial pumps showing promising results is driven by a permanent magnet brush type DC motor. After decoupling from the pump, this motor was tested separately. Data from both experiments was used to obtain performance maps for the pump and the motor.

A finite element two-dimensional quasi-steady state model of the electromagnetic effects in the DC motor was constructed and the results were compared with the experimental results. The resulting model couples geometrical and material property effects to the performance, enabling improved motor design.

## CHAPTER 1 INTRODUCTION

### 1.1 Overview

Direct Methanol Fuel Cells (DMFCs) are a subcategory of Proton Exchange Membrane (PEM) fuel cells, using methanol as compared to hydrogen as a fuel for the direct production of electricity. The DMFC was discovered in 1990 by superacid specialist Dr. Surya Prakash and Nobel laureate Dr. George A. Olah at University of Southern California's Loker Hydrocarbon Research Institute. Since the energy density of methanol is ten times that of compressed hydrogen and fifteen times that of Lithium ion batteries, it alleviates several of the problems of using compressed hydrogen, such as transportability, storage and safety. Owing to the ease of transportation of methanol and its higher energy density, it would seem an ideal replacement for hydrogen-fueled PEM fuel cells. However, the system efficiencies are relatively low due to reduced electrochemical potentials and due to additional transport limitations. Thus the application of direct methanol as a power source is limited to competition with low efficiency systems that demand compactness, such as portable electronics.

DMFCs are available in two design configurations: closed cathode and open cathode. In closed cathode designs, oxygen is made available to the cathode through serpentine channels similar to that of the typical anode, and the exit is coupled to a water extraction system. In open cathode systems, the cathode is open to the atmosphere at the exit. The fuel cell system under study at the DMFC Research Laboratory at the University of Florida power is intended eventually to power commercial laptops and is an open cathode type configuration.

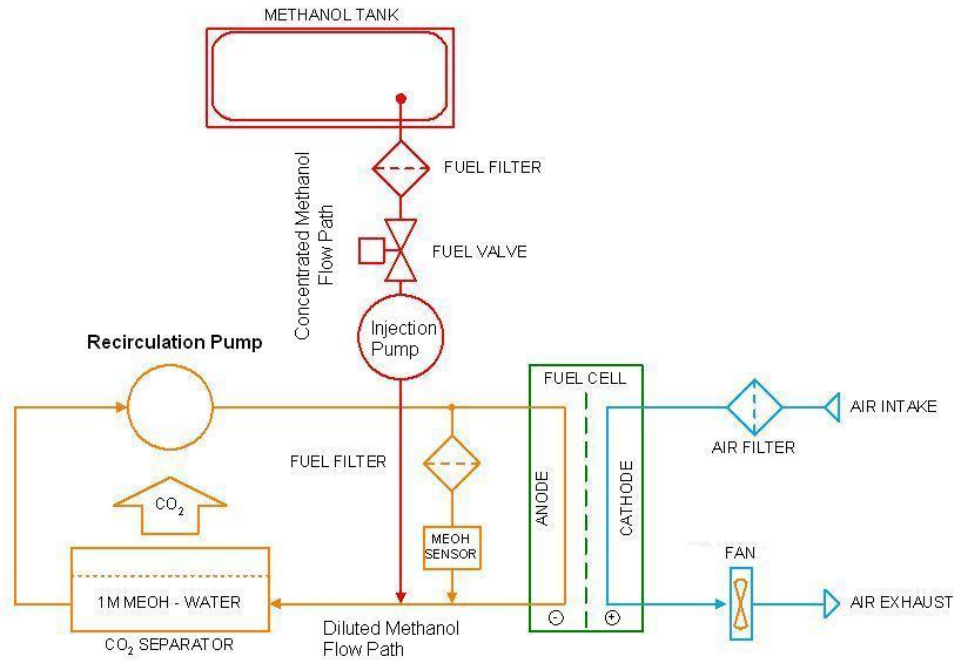


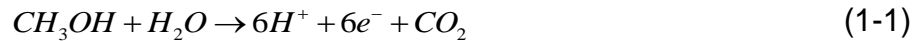
Figure 1-1. DMFC system architecture.

Figure 1-1 shows the architecture of the system. The flow path on the anode side of fuel cell is dilute methanol, with concentrations ranging from 0.5M to 1.2M. Dilute methanol is circulated in the flow path by means of a recirculation pump. A Gas liquid separator, mentioned as CO<sub>2</sub> separator in Figure 1-1, is present in the cathode flow path. The concentrated methanol flow path is used to introduce ultra pure methanol in the cathode flow path using an injection pump. The cathode flow path consists of the open cathode channels, filter, and fans. Purpose of the fan is to provide air at cathode for reaction and cool the cell.

Diluted methanol is oxidized on the catalyst layer to produce carbon dioxide. Water is consumed at anode and produced at cathode. In a open cathode type configuration, the water produced at the cathode permeates back at the anode. This

water balance is extremely crucial in DMFC. Protons are transported from anode to cathode through membrane and electrons are transported through an external circuit, thus driving an electrical load. The cell reactions are,

Anode half reaction:



Cathode half reaction:



Overall cell reaction:



## 1.2 Recirculation Pump

The function of the recirculation pump in a portable DMFC application is to continuously circulate dilute methanol (fuel) in the anode flow path. The recirculation pump should run continuously displacing about 50 ml/min with back pressure of about 3 psi-4 psi. The pump must tolerate bubbles and should be self priming. The recirculation pump should be quiet enough not to be noticed. Since the recirculation pump is driven by the fuel cell, the parasitic power consumption should be as low as possible. Pump components should also be resistant to the corrosion caused by dilute methanol and carbonic acid which is formed when carbon dioxide dissolves in water. Since the DMFC system will be mass produced, the cost of production of individual components, including recirculation pump should be low. Since the pump is operated continuously, the wear on components should be low. Life expectancy of this pump is about 2000-4000 hours.

### **1.3 Goals and Objectives**

To completely analyze the recirculation pump, both wet and dry sides have to be studied. The pumping chamber, check valves, inlet and outlet valves form the wet side, while the actuation mechanism form the dry side. In a different study, the wet side of this pump is being studied and a fluid mechanics model is being developed. The goal of this research is to improve the design capability of pump and motor combination by studying and improving the actuation model. The approach used to achieve this objective is:

- Construct a test apparatus to test off the shelf and in house designed micro pumps components.
- Create a physics based model for a permanent magnet brush type D.C Motor.

The model developed in this study along with the fluid mechanics model will together define a complete pump model.

### **1.4 Thesis Organization**

The remaining portion of this thesis is organized as follows:

Chapter 2 discusses the experimentation apparatus for testing pump and motor coupled together and experimental apparatus to discuss D.C. motor testing.

In Chapter 3, results obtained from pump motor combination tests and from D.C. motor tests are discussed. Various parameters such as flow rate, power consumption and pump-motor efficiency are obtained as functions of differential pressure. Results from D.C. motor tests quantify torque, power consumption and efficiency as functions of rotational speed and energizing voltage. Based on these results, performance of pump is estimated in terms of power consumption and efficiency.

Chapter 4 discusses the modeling of a permanent magnet brush-type D.C. motor. The model dependent variables are identical to those obtained from experimentation, namely torque, power consumption, and efficiency as functions of rotational speed and energizing voltage.

In Chapter 5, validation experiments are described, and the modeling results are validated using the experimental results. The agreement between the experimental data and analytical predictions is discussed in this section of the thesis. In addition, a complete experimental performance map for the pump is presented in this section.

In Chapter 6, conclusions based on experimentation and modeling are presented. Sensitivities regarding various parameters are also discussed in this chapter. Recommendations for future work are also mentioned in this chapter.

## CHAPTER 2 EXPERIMENTATION INVESTIGATION

### **2.1 Pump under Consideration**

#### **2.1.1 Market Research**

Several options for positive displacement micro-pump were considered for potential role of anode recirculation pump. The list includes vane pump, gear pump, screw pump, peristaltic pump and diaphragm pump. Vane pump was eliminated because of the fact that the methanol solution has low lubricity hence the wear of vanes would be of substantial amount. The worn off material from vane can be a potential hazard for the fuel cell stack. Gear pump solves the problem of lubricity. However, the gear pump exhibited poor pump characteristics. As explained later in this thesis, Gear pump has a large slip i.e. drop in flow rate with rise in pressure. During the tests, it was observed that the power drawn to maintain flow rate was much higher than the permissible limit. Peristaltic pump too was eliminated because of its high power requirement.

#### **2.1.2 Candidate Pump**

After conducting a thorough market research diaphragm type pump actuated by a brush type permanent magnet was chosen as a candidate pump because of its extremely small parasitic power consumption while delivering flow rate which is optimum for fuel cell application. The diaphragm pump works on the principle of an oscillating diaphragm member. Actuation is provided by a brush-type permanent magnet D. C. motor. The recirculation pump nominally operates at 45 ml/min at a differential pressure of 1.37 KPa (3 psi), although the purpose on the current investigation is to provide complete information for future design purposes. The

manufacturer rates maximum flow rate achieved by the pump is 70 ml/min and maximum back pressure of 98.04 KPa (14.22 psi). The D.C. motor driving the pump is rated at 6 V and 0.11 A. Concentration of methanol in the anode flow path varies from 0.6 to 1.5 M. Thus the pump should be corrosion resistant to methanol concentration up to 1.5 M.

Another pump in the fuel cell system is the dosing pump, as shown in Figure 1.1. The purpose of this pump is to inject pure methanol in the recirculation loop when the concentration of the methanol in the system drops below a preordained set point decided by the on-board control system. The dosing pump operates nominally at 3ml/min at a differential pressure of 1 psi. Since the manufacturer's data was incomplete, in addition to pump-to-pump variations, it was necessary to build a test rig to quantify the performance of these pumps. Similarly, a special test rig had to be built to determine the performance of the small D.C. motors. The University of North Florida [1], Jacksonville built a micro-motor test rig based on the eddy-current brake phenomenon. These rigs will be discussed in detail in this chapter.

## **2.2 General Purpose Micro Pump Test Rig**

### **2.2.1 Experimental Apparatus**

Figure 2-1 describes the schematic of the general purpose pump test rig with components labeled. Figure 2-2 is an image of the pump test apparatus at UF.

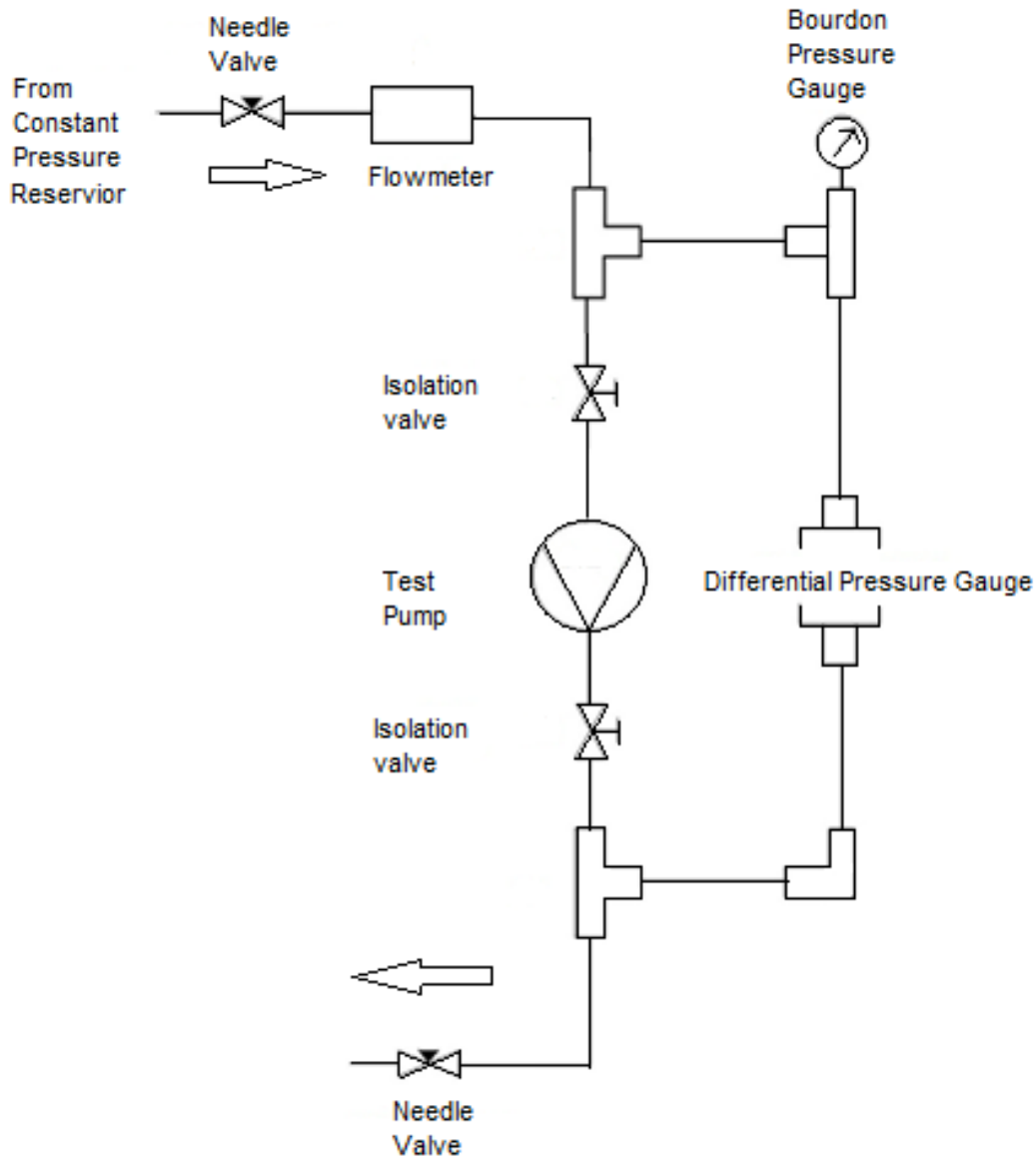


Figure 2-1. Micro-pump experimental facility layout.

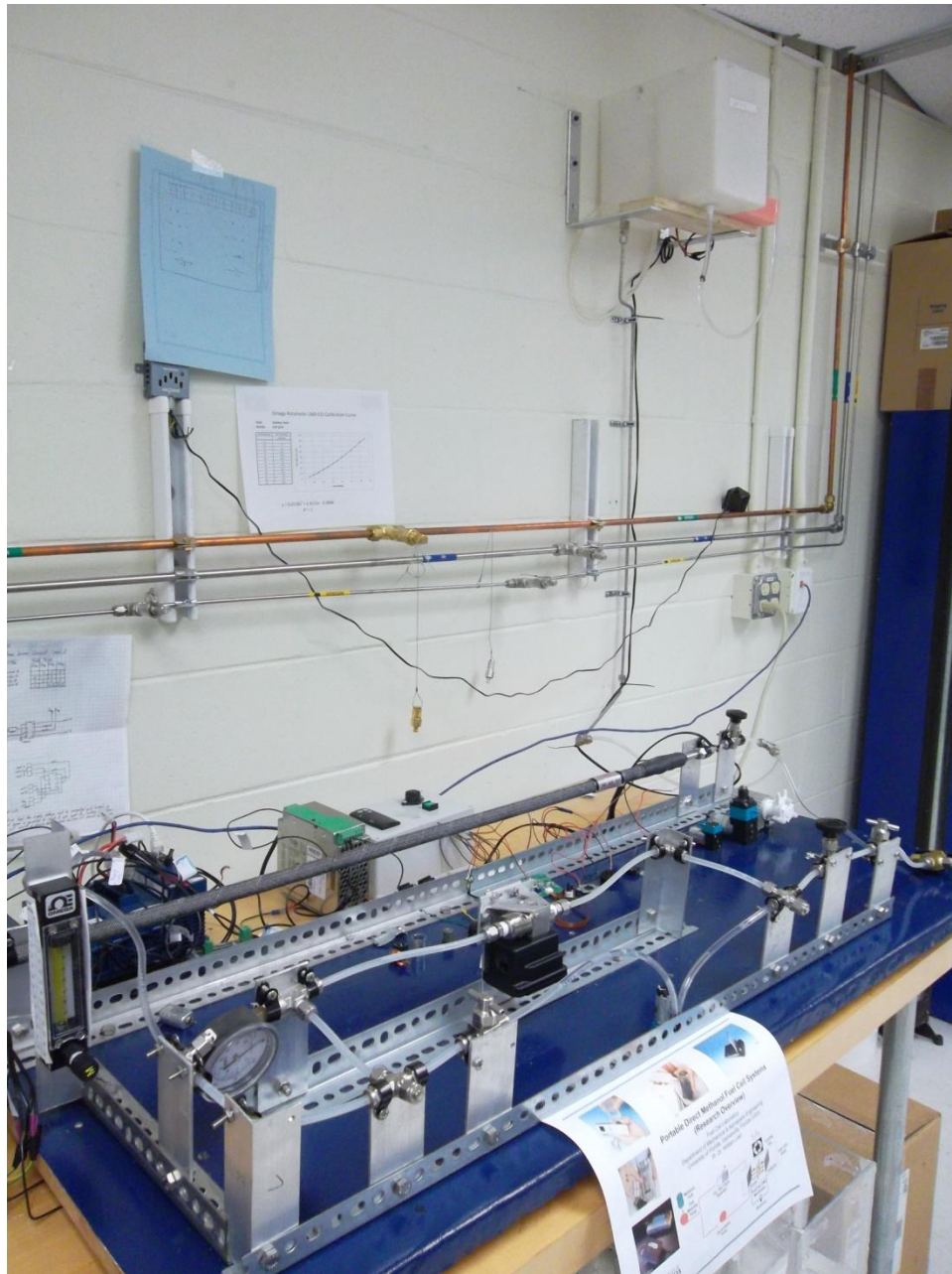


Figure 2-2. General purpose pump test apparatus at the University of Florida.

Water was stored in a constant pressure reservoir located upstream of the pump. Water exited the constant head reservoir through the upstream back pressure valve. An inline flow meter measured the flow rate of the water entering the apparatus. The pressure upstream of the pump was measured using a bourdon pressure gauge. The pressure upstream of the pump was zero at all the times. This is necessary because

different upstream pressures would result in different flow rates for a same amount of differential pressure. Hence all the measurements in flow rates were made with zero upstream gauge pressure as reference. Isolation valves were present upstream and downstream of the pump to facilitate the replacement of the test pump without having to prime the apparatus every time. Pressure across the test pump was measured by a differential pressure transducer powered by an external power supply. Back pressure was imposed on the test pump by using a downstream needle valve. Water exiting the downstream needle valve is directed back to the constant head reservoir tank thus completing the loop.

Following section gives out detailed information on each component.

### **2.2.2 Hardware Components**

1. Needle valve – Needle valve was used upstream and downstream of the pump to adjust the inlet gauge pressure and the back pressure on the pump. Swagelok  $\frac{1}{4}$ " needle valves were used in the apparatus.

2. Flow meter – Inline flow meter is used to measure the flow rate through the pump. The flow meter used is an Omega rotameter, Model number 360-02, with a flow range of 150 ml/min.

3. Isolation valve – Isolation valves were used to prevent water from draining while changing the pumps. The valves and the downstream needle valve were closed when the pump was being replaced.

4. Constant Head Reservoir – The purpose of this tank was to have a constant head at the upstream side of the pump. Water level was maintained at a fixed level above the tube entrance. Without this tank and by using a conventional reservoir at the

suction side, the upstream pressure head would drop as pump operated. To avoid this, a constant head reservoir was devised. Figure 2-2 shows a schematic of the tank.

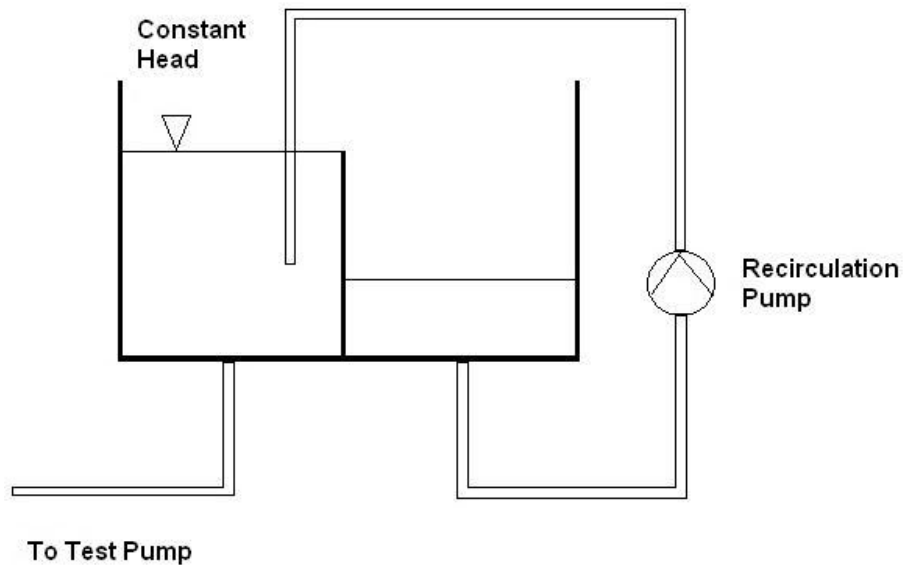


Figure 2-3. Constant pressure head reservoir schematic.

## 2.2.3 Hardware for data acquisition and control of test parameters

### 2.2.3.1 Differential pressure head across the pump

Pressure head across the pump is measured using a differential pressure transducer. In this case, two pressure transducers were used for the measurement. A low range, Omega PX2300-5DI with a range from 0-5psi for low pressure heads and a high range, Omega PX2300-25DI with a range of 0 – 25 for higher pressure heads. Both transducers have a current output in range of 4 – 20 mA. This analog signal was read using LabVIEW software. When pressure gauges were calibrated, it was observed that the pressure versus current relationship for PX2300-25DI was not linear at low differential pressures. Since the operating point for the pump is in the lower pressure ranges, PX2300-5DI was employed in that range. The pressure versus current relationship for this transducer was extremely linear over the entire region of operation.

### 2.2.3.2 Pressure gauge calibration

In the micro-pump test rig, the pressure head generated by test pump is measured by a differential pressure gauge. The output from the gauge, i.e. current, is directly proportional to the pressure difference across the gauge.

Figure 2-4 shows a schematic for pressure gauge calibration.

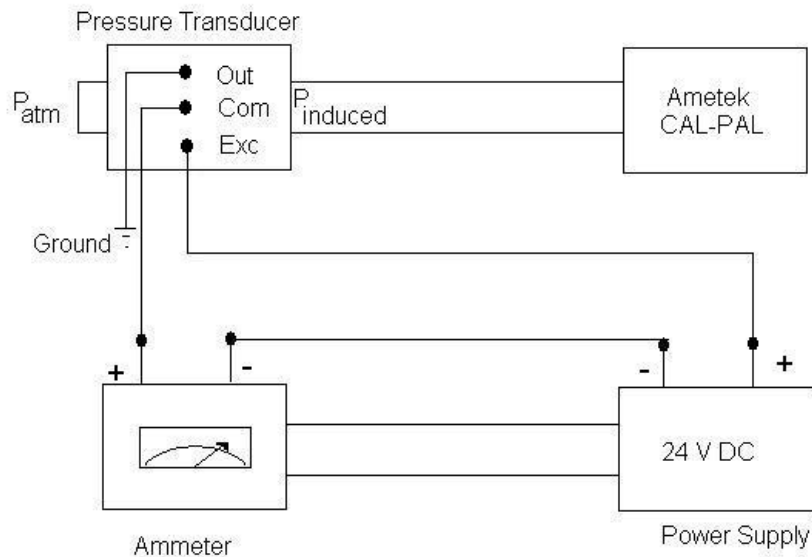


Figure 2-4. Test schematic for differential pressure gauge calibration.

One end of differential pressure gauge is connected to an electronic pressure calibrator. The device used in this case is an Ametek CAL-PAL electronic pressure calibrator. Full scale reading of this device is 200 psi. Accuracy of this device is  $\pm 0.1\%$  of full scale.

An apparatus as shown in Figure 2-4 is constructed. Using the CAL-PAL, pressure is applied to one end of differential pressure gauge and corresponding current reading is noted on an ammeter. Pressure is gradually increased from 0 psi till maximum pressure of the gauge. Then, pressure is gradually released till 0 psi is reached. By

following this method, back-lash error is avoided. The data obtained for pressure and current is then plotted and a curve fit is obtained for the particular data set.

Two pressure gauges were used in the pump testing. One with a pressure range from 0-5 psi and other with range from 0-25 psi. The reason to employ 0-5 psi gauge is that, the accuracy of the 0-25 psi pressure gauge is small at lower pressures. To avoid these errors, a gauge with lower range was used whenever a low pressure tests were performed. Both the gauges were manufactured by Omega. Pressure  $P$  is expressed in term of current  $I$  by following equations.

#### **2.2.3.3 Differential Pressure Gauge Calibration curves**

$$0-5 \text{ psi:} \quad P = 0.3206 \times I - 1.4506 \quad (2.1)$$

where pressure  $P$  is measured in psi while current  $I$  is measured in mA.

$$0-25 \text{ psi:} \quad P = 1.5802 \times I - 6.034 \quad (2.2)$$

#### **2.2.3.4 Upstream pressure**

Upstream pressure is measured using a Bourdon gauge that reads gauge pressure.

#### **2.2.3.5 Flow rate**

Flow rate through the pump is measured by an inline flow meter in series with the pump. Most inline flow meters cause a pressure drop across them. Hence the placement of the flow meter in the test rig might be crucial. In the scenario where the flow rate meter is placed downstream of the test pump, when the needle valve is fully open the exit of the flow meter is at ambient pressure. The exit of the pump is at the same pressure as that of the flow meter entrance, which is higher than ambient pressure. Hence the pump can never be tested at truly zero pressure head condition. Hence the flow meter has to be placed upstream of the pump.

### **2.2.3.6 Flow meter calibration**

Calibration data for this inline flow meter, an Omega Rotameter, was provided by the manufacturer. The flow meter used has a 65 mm scale and has accuracy of  $\pm 2\%$  of full scale deflection. Flow rates up to 150 ml/min can be measured by this Rotameter. Using the calibration data provided, a curve fit was achieved with an  $R^2 = 1$ . Flow rate  $F$  is expressed in term of scale reading  $R$  by Equation (2.3)

$$F = 0.0139 \times R^2 + 1.4112 \times R - 0.3846 \quad (2.3)$$

where  $F$  is measured in ml/min.

### **2.2.3.7 Actuation voltage**

The actuation voltage is provided by the D.C. power supply rated at 24 V and 5 W. The voltage is measured using National Instrument data acquisition systems. The data is logged using the LabVIEW software.

### **2.2.3.8 Current to drive the pump**

Depending on the back pressure imposed on the pump, the motor draws the current to drive the pump. This current can be measured by National Instruments data acquisitions system by employing a precision shunt resistor. This data is logged using the LabVIEW software.

### **2.2.3.9 Motor speed**

Motor speed or motor frequency was not measured. However the current consumed by pump and motor was recorded. DC motor tests were carried out separately to identify the relation between motor current and rotational speed.

### **2.2.3.10 Data acquisition**

The data acquisition system employed to retrieve the data was a National Instrument Compact FieldPoint. The data acquisition system has two analog input, two analog outputs and thermocouple input and pulse width measurement module.

Pump voltage and pump current was acquired using analog input module. Current generated using differential pressure gauge was acquired using an analog input module. In the formula node of LabVIEW, calibration curves were entered and thus readings of differential pressure were obtained for the respective current signal generated. Depending on the pressure transducer used, the calibrations equations were modified. Flow meter readings were manually entered in the excel sheet and the curve fit equation was used to obtain the flow readings. Current was measured using a precision shunt resistor. Appendix 1 describes the experimental uncertainty in measuring voltage and current.

### **2.2.4 Test Procedure**

In an actual test, water stored in the constant pressure reservoir entered the apparatus through the upstream back pressure valve. The entire apparatus was primed and ensured that no air bubble was present in any part of the apparatus. Power sources for data acquisition system and differential pressure transducer were set to 24V. Both the upstream and the downstream needle valve were completely open. Power source for test pump was set to a desired energizing voltage. The pump was turned on by activating its power source. As the pump started operating, upstream pressure rises. The upstream needle valve was adjusted in such a way that the bourdon gauge read zero gauge pressure. The pump was allowed to run in this state till steady state was achieved. Voltage across the motor, current flowing through the motor and the

differential pressure across the pump was recorded using the LabVIEW VI. Flow rate readings were manually recorded. Later, the back pressure valve was adjusted in such a way that the differential pressure gauge read a pressure 0.5 psi higher than the earlier test. It was ensured that upstream gauge pressure was zero by adjusting upstream needle valve. The procedure was repeated until the downstream needle valve is completely closed or the test pump stalls, whichever happens earlier.

### 2.2.5 Data Reduction

Flow meter scale readings are then entered for every test point. Using calibration Equation (2.3), flow meter readings in ml/min are calculated. Flow rate, Q is measured with a Rotameter. Pressure is calculated using Equation (2.1) and Equation (2.2), depending on the pressure range the pump is being tested. Input power  $P_{IN}$  is given by,

$$P_{IN} = V \times I \quad (2.4)$$

where  $P_{IN}$  is measured in Watt, voltage V is measure n Volt and current I measured in Ampere. Output power  $P_{OUT}$  is given by,

$$P_{OUT} = (\Delta P \times 6894.757) \times \left( \frac{Q \times 10^{-6}}{60} \right) \quad (2.5)$$

where  $P_{OUT}$  is measured in Watt, differential pressure  $\Delta P$  is measured in Ampere and then equivalent pressure is achieved using calibration Equation (2.1) and Equation (2.2). The units for pressure in this equation is psi and flow rate Q is measured in ml/min. The Efficiency  $\eta$

$$\eta = \frac{P_{OUT}}{P_{IN}} \quad (2.6)$$

Results were achieved for flow rate, power consumption and efficiency as functions of the differential pressure. These results are discussed in the next chapter in form of plots.

### 2.3 D.C. Motor Test Setup

The pump testing rig was developed in-house at the University of Florida, while the test rig for D.C. motor was constructed by the Mechanical Engineering Department at the University of North Florida. Figure 2-5 shows an image of the schematics of the apparatus. Figure 2-6 shows a closer view of the micro-dynamometer.

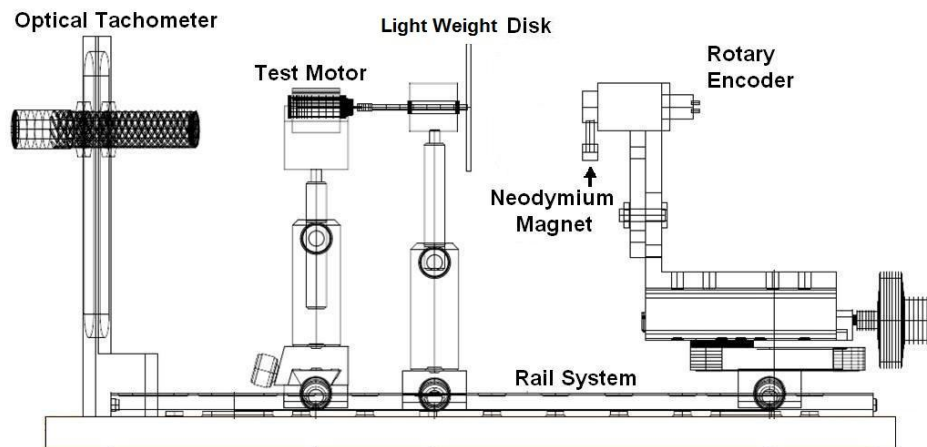


Figure 2-5. Motor Test Rig developed at University of North Florida.

An eddy current dynamometer design is used to test the motor. The motor speed is measured using an optical tachometer. The dynamometer can be used for motors with power less than 4W.

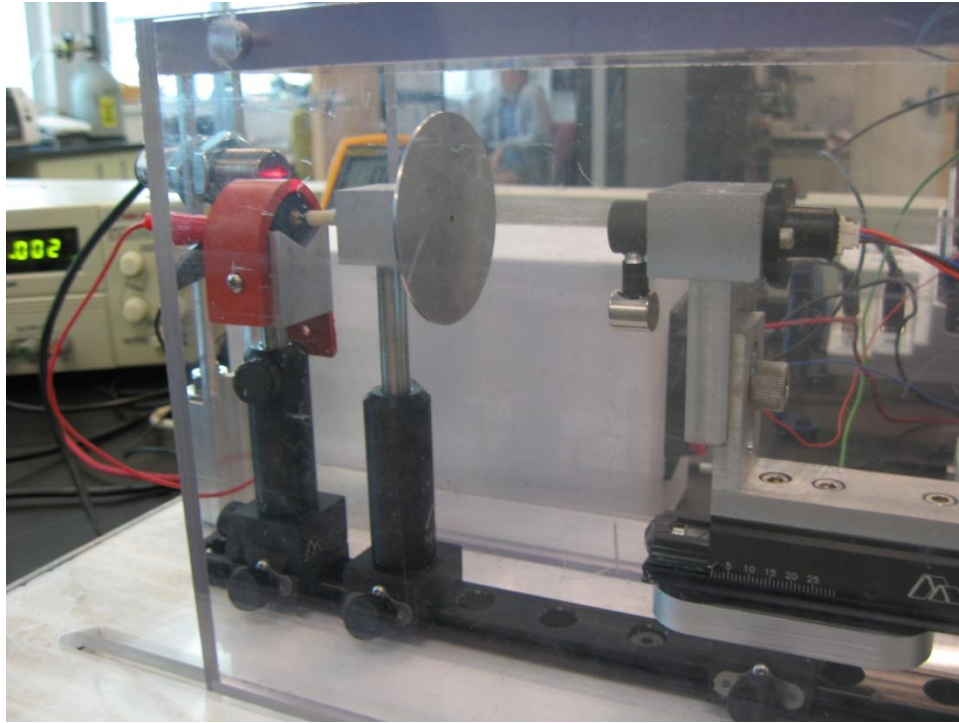


Figure 2-6. Micro-dynamometer in operation at the University of North Florida.

## **2.3.1 Hardware Components**

### **2.3.1.1 Rotating assembly**

Rotating assembly consists of an aluminum disk driven by the test motor. Since torque produced by these motors is extremely small, a very light weight disk is required. The specifications for the components used in the micro-dynamometer can be found in the project report for the micro-dynamometer [1]

### **2.3.1.2 Pendulum assembly**

As the motor rotates the aluminum disk, torque is transmitted back to the source of magnetization. This causes the pendulum to rotate. Torque induced is calculated by measuring the weight of the pendulum assembly and the angle of rotations. Neodymium magnets are used in this application because of the magnetic potential and low weight.

## **2.3.2 Hardware for Data Collection and Control of Test Parameters**

### **2.3.2.1 Optical tachometer**

An optical tachometer was used to measure the speed of the rotating disc. The optical tachometer used in this application is Monarch ROS-W. Maximum speed that can be measured by this tachometer is 250,000 RPM and has a TTL output signal.

### **2.3.2.2 Rotary encoder**

An encoder was used to measure the angular position of the pendulum, thus estimate the torque. The rotary encoder used in this application is US Digital MAE3. The encoder has a resolution of 8192 counts/rev and has output of 12 bit PWM signal.

### **2.3.2.3 Current shunt**

Current consumed by the motor is measured by measuring the voltage across a current shunt. The current shunt used in this application is manufactured by Packet Flux Technologies and is rated at 0.5A and 100 mV.

### **2.3.2.4 Data acquisition**

National Instrument CompactDAQ – NI 9401 is a digital input/output module and is employed to acquire encoder and tachometer signals. NI 9215 is an analog input module and was employed to acquire motor voltage and motor current. Software – National Instrument LabVIEW is the data acquisition tool used in this case. The Virtual Instrument (V.I.) was created by students at the University of North Florida.

## **2.3.3 Test Procedure**

The motor drove a non ferrous disc, aluminum in this case, which rotated in a magnetic field generated by a neodymium magnet. The proximity of the rotor to the permanent magnet affected the motor loading. The resistive torque on the motor increased as the disc approached the neodymium magnet. The magnetic field

interaction with induced eddy current in the disc causes the pendulum to deflect. The direction of deflection is given by Fleming's left hand rule. The deflection of the pendulum was measured using an optical encoder. Initially, the pendulum assembly was kept at the distance farthest from the disc. The rail system was used to adjust the distance between different mounts. The distance between pendulum assembly and disc was gradually rotated and the resulting drop in the motor speed was noted in the LabVIEW VI. Once the speed dropped by 100 rpm, the pendulum assembly was locked in the position, and the motor was allowed to run for some time to achieve steady state. Torque is calculated as a function of the deflection of the pendulum assembly. Once the torque versus time curve achieved steady state, data logging was turned ON. Data comprising of motor current, motor voltage, deflection of pendulum and motor speed was noted. Data logging is kept turned ON for about 5 seconds so that sufficient data points are available for each test point. The data achieved for those five seconds is averaged out to obtain a unique data point.

## **2.3.4 Data Reduction**

### **2.3.4.1 Angle of deflection of the pendulum**

The angle of deflection of the pendulum is measured using a rotary encoder. The output of an encoder is 12 bit PWM signal. Using NI 9401 Digital I/O module, width  $w$  of the pulse generated by the encoder is measured. Angle of deflection  $\theta$  in degrees is then given by,

$$\theta = \frac{w}{4096} \times 360 \quad (2.7)$$

### 2.3.4.2 Torque

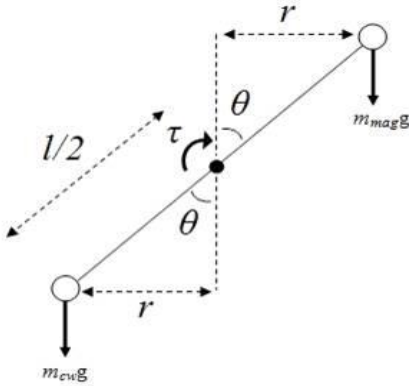


Figure 2-7. Torque acting on a pendulum system comprising of magnet and counter weight [1].

Torque  $\tau$  is calculated by applying law of conservation of angular momentum and is given by

$$\tau = g \times \frac{l}{2} \times \text{Sine}(\theta) \times (m_{CW} - m_{Mag}) \quad (2.8)$$

where 'g' is the acceleration due to gravity in m/s, l is length of pendulum in meter,  $\theta$  is angle of deflection measured in radians.  $m_{CW}$  is the counter weight mass attached to the pendulum and  $m_{Mag}$  is the mass of the neodymium magnets.

### 2.3.4.3 Motor speed

Motor speed is measured by a remote optical tachometer. The sensor is powered by an external power supply and generates a negative pulse every of time light emitted by sensor bounces off the reflective tape on the disk.

### 2.3.4.4 Input power

$$P_{IN} = V \times I \quad (2.9)$$

where  $P_{IN}$  is measured in Watt, Voltage V is measure n Volt and Current I measured in Ampere

#### 2.3.4.5 Output power

Output power for a motor is given a product of its rotational speed and the torque generated.

$$P_{OUT} = \tau \times \omega \quad (2.10)$$

#### 2.3.4.6 Efficiency

Efficiency  $\eta$  is defined as

$$\eta = \frac{P_{OUT}}{P_{IN}} \quad (2.11)$$

Data achieved from the DC motor tests using the micro-dynamometer is the Torque, power consumption and efficiency as functions of energizing voltage and motor speed. These results are discussed in detail in the next chapter.

## CHAPTER 3 EXPERIMENTAL RESULTS

The KNF pumps driven by a permanent magnet brush- type D.C. motor were tested using the general purpose pump motor combination test rig described in Chapter 2. The D.C. motors were then tested separately using the motor test rig developed at the University of North Florida. Experimental uncertainty associated with each test has been discussed in Chapter 2. Using the data from these two test apparatus, performance of the pump was inferred and can be used for modeling the fluid mechanics. The electromagnetic model developed in Chapter 4 using the finite element method is validated using the experimental data obtained from the D.C. motor test. Results obtained from both of the rigs will be discussed in detail in this chapter.

The motor driving the KNF pump is rated at 6V and 0.11 A. It is desirable to evaluate the performance of the pump motor combination at its rated specifications. Hence 6V was selected as one of the actuation voltage. As discussed in Chapter 2, the flow rate design requirement for the recirculation pump 45 ml/min with a back pressure of 3 psi. This operating point was achieved when the pump was run with energizing voltage of at least 4V. Hence this voltage was selected as the other energizing voltage. The desired operating point cannot be achieved by energizing the pump with a voltage less than 4V.

### **3.1 General Purpose Micro Pump Test Rig**

Using the general purpose pump test rig, characteristics of pump and motor combination like flow rate, power consumption and efficiency as a function of differential pressure were measured. Tests were run under different environmental conditions and

by different operators. Figure 3-1 shows a plot of flow rate (ml/min) versus the differential pressure (psi).

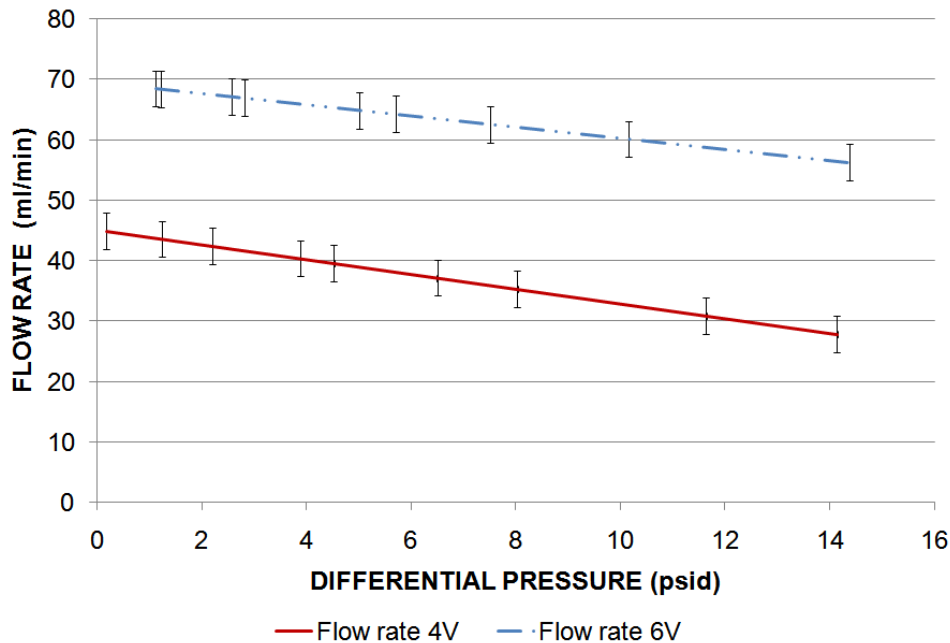


Figure 3-1. Plot of flow rate of KNF pump as a function of differential pressure.

For a positive displacement pump like KNF, the flow rate should ideally remain constant independent of back pressure, as long as the frequency and stroke are constant. The working principle of a KNF can be visualized by a piston inside a cylinder. As the inlet cavity of the pump expands, a low pressure region is created and this region should be ideally filled by the fluid from the inlet line. If the valves do not seal outlet line as desired, the fluid from outlet line fills up this region. This causes the net flow at the outlet to drop. This drop in flow rate is called as Slip. As the back pressure increases, performance of valve drops, thus causing increase in slip.

As the differential pressure rises, the force required to push the fluid rises as well. This causes the motor torque to increase with it. The motor speed, according to the torque-speed characteristics, drops thus the pump flow rate drops with it causing a slip.

This physical phenomenon can be seen in Figure 3-1 for both 4V and 6V. The slip should be as low as possible for a positive displacement pump as it affects the overall pump performance. When the pump is energized by 4V, a slip of 16% was observed at 3 psi and 40% at 14 psi. When the pump was energized by 6V, a slip of 2.4% percent was observed at 3 psi and 17% at 14 psi. The plots are derived by using linear fits to actual test data.

Figure 3-2 shows a plot of the power consumption and efficiency (percent) versus the differential pressure (psi).

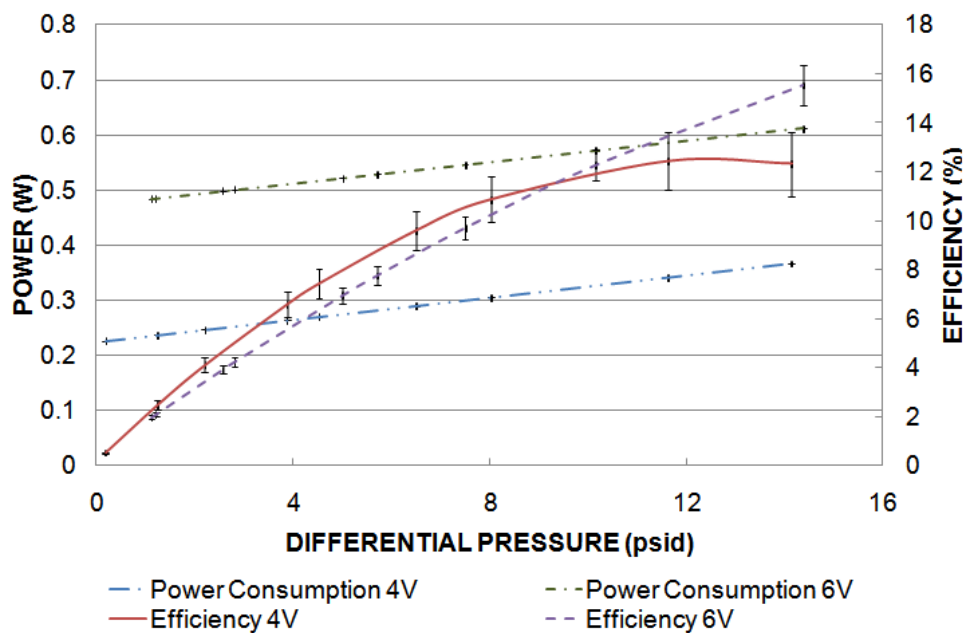


Figure 3-2. Plot of efficiency and power consumption of KNF pump as a function of differential pressure at two actuation voltages.

Efficiency of the pump motor combination is slightly higher for 4V energizing voltage at lower differential back pressure. As the back pressure increases, the pump becomes more efficient when operated at 6V. The pump motor combination is more efficient in lower back pressure region when operated at 4V because the power input is significantly smaller even if the slip is higher for 4V. As the back pressure rises, the

advantage of lower input power drops as compared to higher losses because of slip. Thus the pump motor combination becomes efficient at higher back pressure region when operated at 6V because the slip is comparatively small even if the input power is higher.

Energizing voltage and current drawn by the motor are logged using National Instrument Compact Field point data acquisition system as explained in Chapter 2. Accuracy of these devices is extremely high and hence the uncertainty in measuring the power consumption is extremely low. The efficiency measurement depends on the flow rate measurement. The device used for flow rate measurement, a rotameter, has comparatively higher uncertainty. Also the error in measuring flow rate is higher at lower flow rates. For this reason, the uncertainty in efficiency measurement increases as back pressure rises or flow rate drops.

In case of fuel cell application, the pump should consume less power rather than being efficient at the design operating point. For this reason, it is advisable to operate the pump at lowest possible voltage that meets the design requirement i.e. 4V in this case.

### **3.2 D.C. Motor Test Rig**

As explained earlier, the D.C. motors were tested so that the experimental data obtained can be used to validate the electromagnetic model developed later in Chapter 4. Using the D.C. motor test rig, characteristics of motor like torque, power consumption and efficiency as a function of rotational speed are measured.

Figure 3-3 shows a plot of torque as a function of rotational speed.

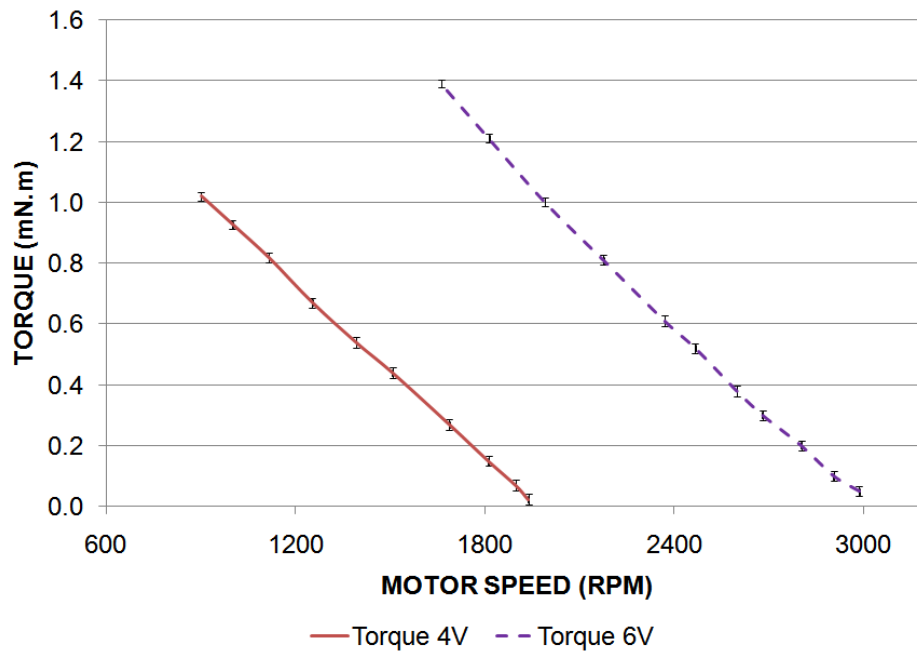


Figure 3-3. Plot of Torque as a function of rotational speed

For D.C. motor, torque varies linearly with motor speed. This trend can be seen in Figure 3-3 for both the actuation voltages. Uncertainty associated with the torque measurement is because of the uncertainty associated with measuring the angular position of the pendulum assembly. Uncertainty is highest at the lower torque readings because the angular deflection of the pendulum is very small, hence the error associated in angle measurement becomes comparable to the angle measured. The connection between motor and aluminum disc is made by flexible coupling. Measures are being taken during experimentation to minimize eccentricity to the maximum possible extent. However, some eccentricity would exist in the coupling. The uncertainty associated with this eccentricity is not discussed in this study. The experimental no load speed achieved when the motor was energized by 4V was 1966 rpm and for 6V was 2993 rpm. The optical tachometer measures the speed with accuracy of 0.05% of

the reading. Hence the error associated with these readings would be approximately 1-1.5RPM.

Figure 3-4 shows a plot of current drawn by the motor and its efficiency as a function of motor speed.

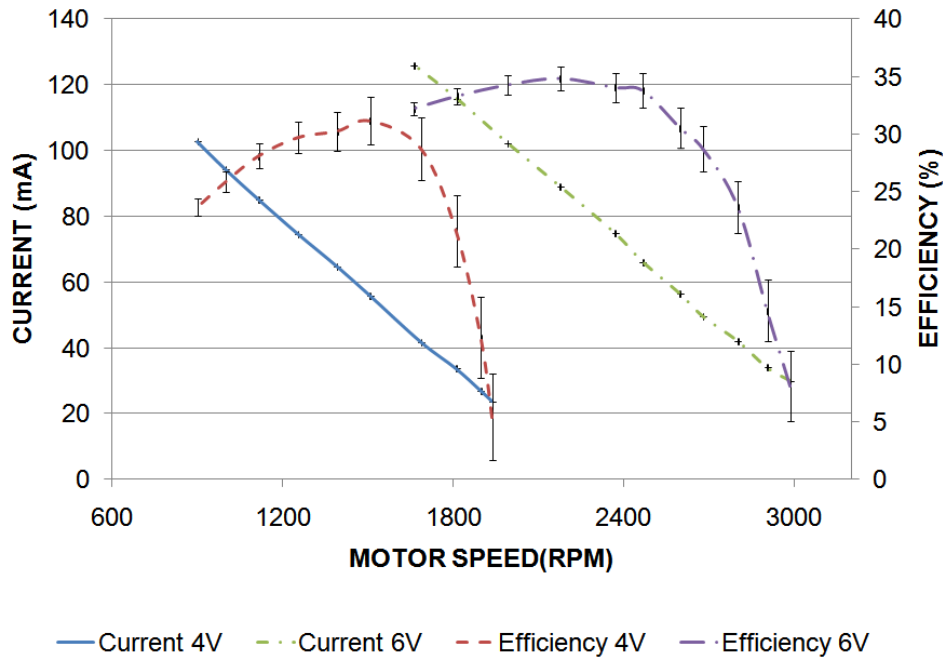


Figure 3-4. Plot of current and efficiency as a function of rotational speed

Like torque, current drawn by the motor is also linearly proportional to the motor speed. The linear nature of the current-speed relation is governed by the DC motor theory. And the trend of the result is as expected. Stall current observed for 4V is about 169 mA and for 6V is about 249 mA. From these values, resistance of the motor can be calculated. The terminal resistance is thus approximately 24 ohm. Resistance can also be calculated by physically measuring the resistance across the brush and rotating the shaft. It was observed that average resistance over a complete cycle was 25.3 ohm. Each brush contributed 0.3 ohm resistance. Thus resistance across coils was 24.7ohm,

which agrees with experimental data within the experimental uncertainty. An error of 3% was seen in resistance calculated. The efficiency plot follows an expected parabolic profile. For 4V, peak efficiency achieved was about 31% at the speed of about 1500 rpm. For 6V, peak efficiency achieved was 35% at the speed of 2176 rpm. The current in motor test rig was logged using a precision current shunt and National Instrument analog input module 9215 with accuracy of  $\pm 0.02\%$ . Hence the uncertainty in current measurement is extremely small. The efficiency measurement, however, depends on the measurement of torque and rotational speed. Since the uncertainty in measuring torque is higher at lower speed, we see a higher uncertainty in efficiency measurement at lower motor speed. The uncertainty drops as the motor speed increases.

### 3.3 Experimental Results for Pump

Torque versus speed and current versus speed curves were obtained for the D.C. motor from the motor test apparatus. Thus, torque versus current plot can be deduced from both of these data sets. Figure 3-5 shows this plot.

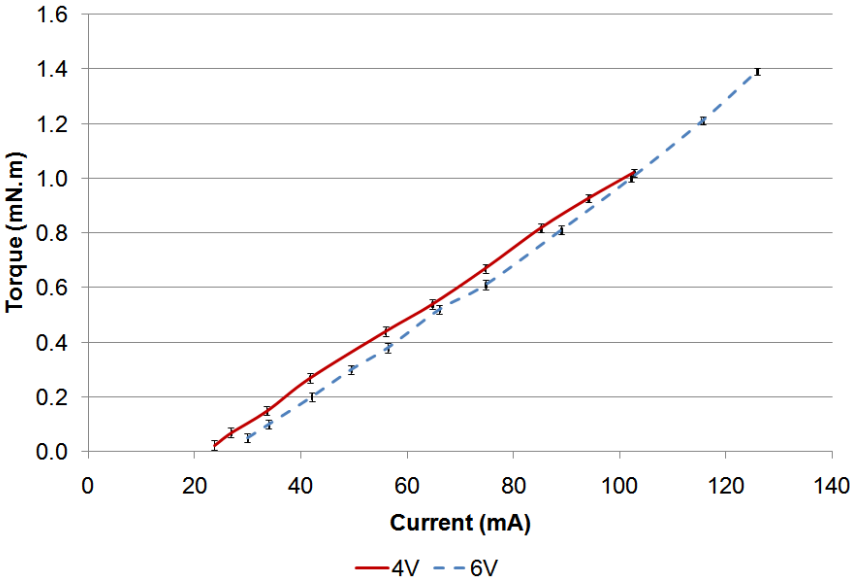


Figure 3-5. Plot of torque versus current for the experimental data

From Figure 3-5, it can be seen that torque is linearly dependent on the current drawn by the motor. Within the regime of experimental error, it can be said for a given amount of current flowing through the coils, only a certain constant amount of torque will be generated. The energizing voltage dictates the speed at which this torque is available. A linear curve fit can be obtained for torque and current relationship. From pump motor tests, data for the current drawn by the motor for varying pressure is also available, thus the motor torque can be related to the differential pressure. Using these relations and Equation 3.1, pump efficiency and differential pressure can be correlated.

$$\eta_{overall} = \eta_{pump} \times \eta_{motor} \quad (3.1)$$

Figure 3-6 shows a plot of pump efficiency as a function of differential pressure.

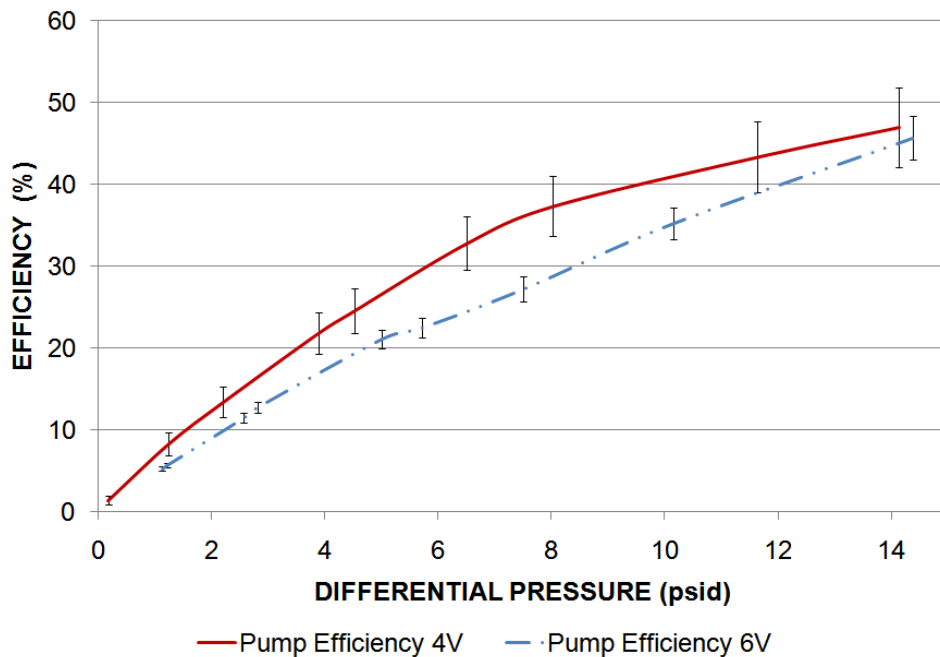


Figure 3-6. Plot of pump efficiency as a function of differential pressure.

Uncertainty associated with pump efficiency measurement exists because of the uncertainty in measurement of the flow rate. As explained earlier, higher the back pressure, lower the flow rate thus higher the error. From experimental results, it can be seen that the pump is marginally efficient when operated at 4V. The results obtained for the pump chamber gives an indication of the pump hydrodynamic efficiency. This data can be used to validate hydrodynamic efficiency of the pump.

## CHAPTER 4 D.C. MOTOR MODEL

A KNF pump was tested at the University of Florida's general purpose pump testing rig and the motor driving the pump was tested at University of North Florida's D.C. motor testing rig. Using the experimental data from both of these tests, experimental data for the pumping chamber was also obtained. To support the modeling efforts on the pump, a steady state model for the D.C. motor is generated. This chapter will focus on discussing the physics of a permanent magnet brush D.C. motor and the model in detail. The purpose of this model is to relate the physical dimensions and material properties of motor components to the performance map, thus contributing to design optimization.

The finite element method is used to model the electromagnetic actuation of the motor. A magnetostatic or steady state magnetic simulation is presented in this thesis. Flux linkage in each coil and torque produced a function of current in coils, current at the terminal and position of the rotor is calculated.

### **4.1 Need for Finite Element Analysis**

Maxwell's equations are a set of partial differential equations which describe how charges and current interact with electromagnetic field. The forces acting on charge are given by the Lorentz law. Flux density, electromagnetic field intensity, force and torque can be calculated by solving these equations. However, to solve these equations analytically, geometry has to be comparatively simple. The equations become extremely difficult to solve if geometry becomes complicated. In case of a brush type permanent magnet D.C. motor, the geometry of components is extremely complex. Also, components are made of dissimilar materials thus making the analytical analysis

difficult. To identify the performance of the motor at different rotor positions, the equations would have to be solved with different initial and boundary conditions.

Finite element method can be used for solving extremely complex geometries. Approach to solve the problem does not alter when initial conditions or boundary conditions are changed. This is extremely helpful for calculating motor parameters for different orientations are coil currents.

## **4.2 Finite Element Method Magnetics**

Finite element package used in this study is an open source package called Finite Element Method Magnetics or FEMM [2]. This package is used to solve two dimensional planar or axisymmetric problems. This package can, however, solve only steady state low frequency problems. Thus this package is well suited for the problem under consideration. This package will be used to calculate torque generated by the rotor as a function of coil current and position of the rotor. The results obtained will be then compared with experimental results for this motor. The relevant partial differential equation governing the solution scheme can be found in the FEMM manual [2]

## **4.3 Application of FEMM to D.C. Motor Model**

### **4.3.1 Pre-processing**

Pre-processing step involves defining the geometry of the model, adding material to the components and applying the boundary conditions.

Figure 4-1 shows model of D.C. motor with dimensions exactly equal to the actual dimensions. The model is generated using graphical pre-processor integrated in the FEMM package.

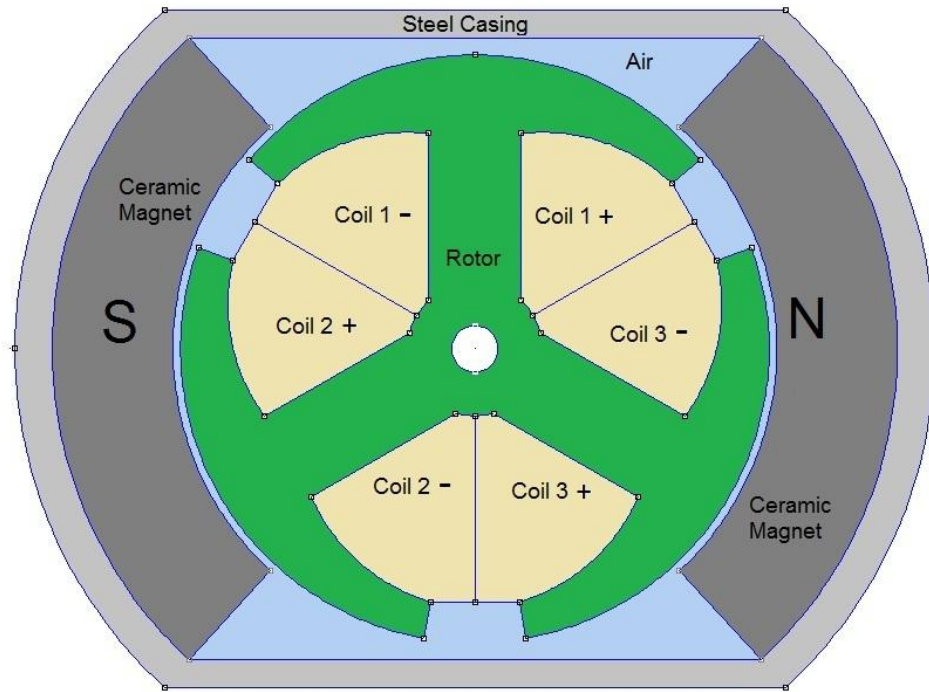


Figure 4-1. FEMM Model of permanent magnet brush type D.C. motor with graphic illustration.

The position of rotor with respect to the permanent magnet depicted in Figure 4-1 is defined as a 'Reference Position'. Any use of this term in this thesis should refer to the position of rotor as in Figure 4-1. It can be seen in Figure 4-1 that a sign exists next to a coil indicate the direction of the coil winding. Positive indicate that the current in the coil is coming outside the plane of paper, while negative indicate that current in the coil is going inside the plane of paper. With this particular schematic, if positive end of power source is connected to coil 1 and negative terminal partially to each of coil 2 and coil3, the rotor will rotate in clockwise direction. The indicated position of rotor in Figure 4-1 is a reference zero position. Appendix 2 has a detailed geometry of the components with dimensions. Figure 4-2 shows the commutator and brush arrangement for this motor.

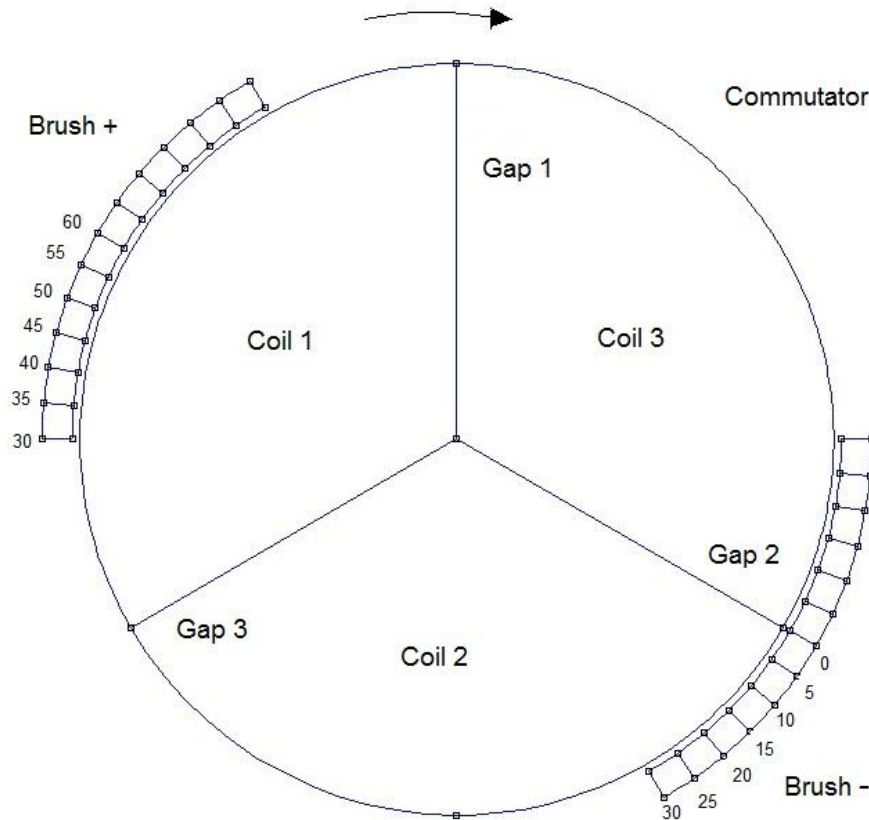


Figure 4-2. Commutator brush arrangement for D.C. motor.

The marking on the brush indicate the rotation for reference zero position in counter-clockwise direction. The position of brush with respect to commutator dictates the current flowing through the coil in contact. For a given reference zero position, Coil 1 will be energized with positive current and magnitude equal to the magnitude of terminal current. Negative current will be applied to Coil 2 and Coil 3 and magnitude equal to half the magnitude of terminal current. Thus Coil 2 and Coil 3 will be partially energized. If a brush is in contact with two coils, the current is divided equally between both the coils.

It can be seen from the Figure 4-2 that for 30 degrees counter-clockwise rotation, Coil 2 will lose contact with both the brushes. Thus Coil 2 will be de-energized. This is a desired effect, because after 30 degrees rotation, angle between North Pole of magnet

and Coil 2 will be zero. Thus any amount of current in Coil 2 will not contribute towards generation of torque, since the angle between external magnetic field and current flow is zero, the cross product of these two quantities will be zero, thus zero force acting on the coil. Equation 4.1 governs this phenomenon. However, maximum possible torque will be generated from both Coil 1 and Coil 3, since Coil 1 will be attracted to South Pole and Coil 3 will be repelled by the South Pole.

Table 4-1. Description of DC motor components

Component	Quantity	Material	Description
Rotor	1	M-19 Steel	Laminated plates
Coil	3	Copper	Wire diameter: 0.16 mm Turns: 120 turn each
Permanent Magnet	2	Ceramic	Horse shoe type
Casing	1	1018 Steel	-

**4.3.2 Boundary Conditions**

The problem analyzed in this report is a planar problem, with a boundary surrounding the geometry. The boundary is modeled in a way to simulate open space. Compared to the model geometry, the boundary is comparatively larger in size and thus models open space fairly accurately. Figure 4-3 shows a representation of motor and the boundary.

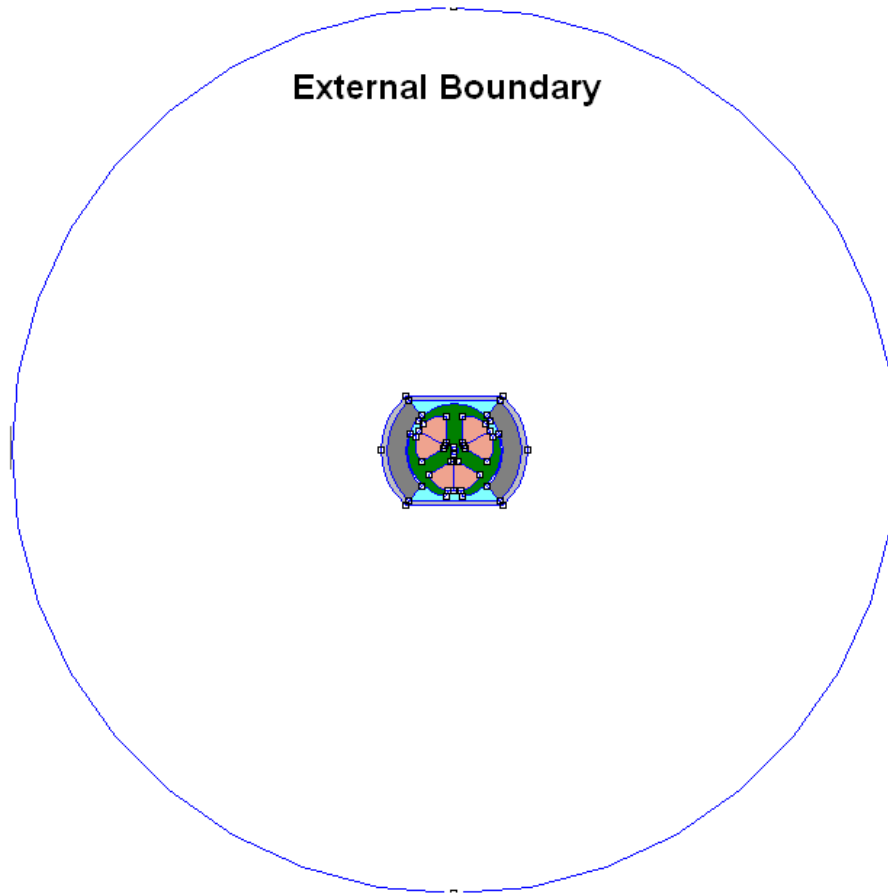


Figure 4-3. Comparison of the external boundary and the motor size.

Equation 4.1 gives the mathematical representation of the boundary condition used in this problem and is applied to the circular section tagged as External Boundary in Figure 4-3.

$$A = 0 \quad (4.1)$$

where  $A$  is a magnetic vector potential. By defining  $A=0$ , we disallow magnetic flux lines to cross the boundary. Thus the magnetic flux lines are always parallel to the boundary.

### 4.3.3 Mesh Generation

FEMM utilizes a triangular element for computation of flux density and flux intensity. The triangular elements are created by an inbuilt program called 'triangle.exe'. Figure 4-4 shows the geometry of model with triangular mesh.

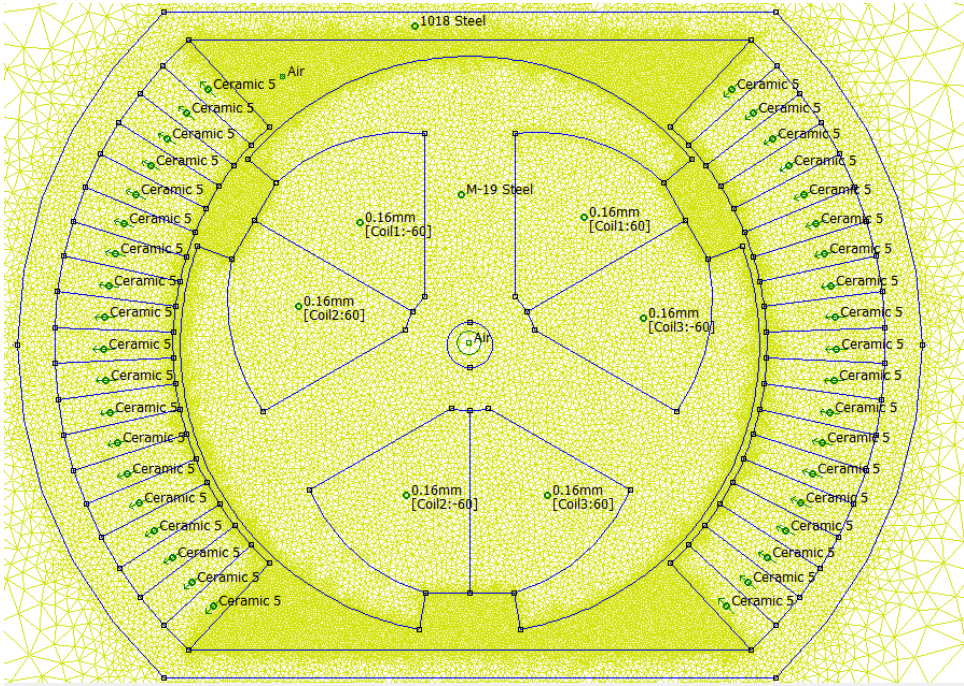


Figure 4-4. Triangular mesh in the motor geometry.

In Figure 4.4, it can be seen that permanent magnets are modeled as a collection of small individual magnets. This scheme is advantages compared to modeling them as single block because with this scheme the magnetization direction can be controlled more accurately. In this case, magnets have a radial magnetization direction. The direction of arrow on each block illustrates the direction of magnetization. Thus, the magnet on the left of the rotor is modeled as a North Pole while one on the right is modeled as a South Pole. Total number of elements in this model is 215,769 and total number of nodes is 107,933. Figure 4.5 gives a closer look at the air gap between the rotor and the magnets.

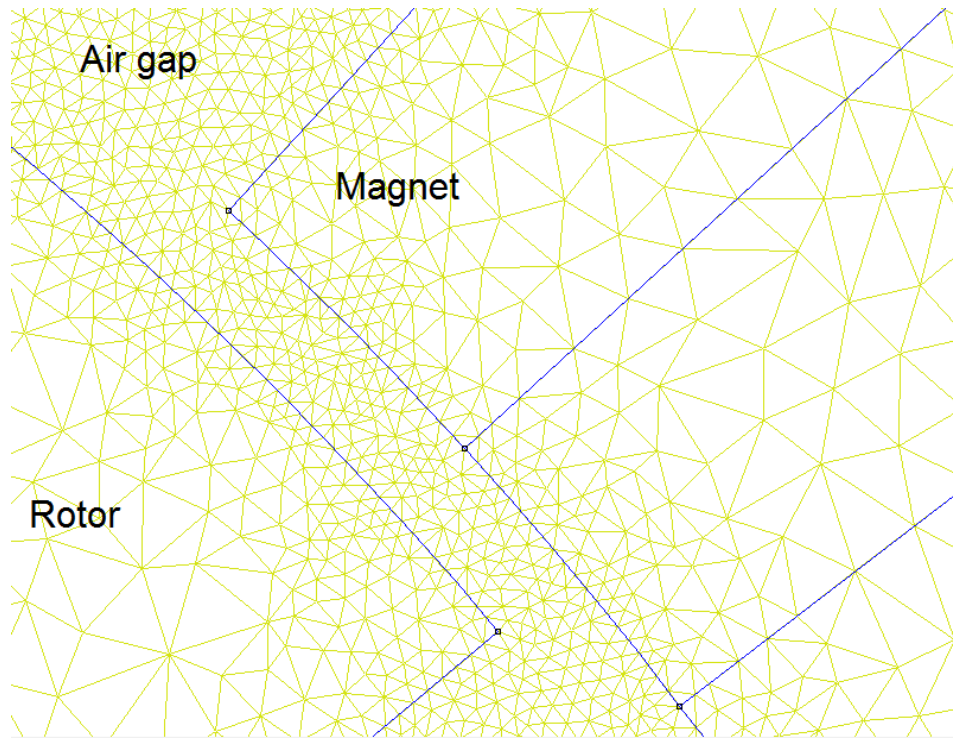


Figure 4-5. A closer view at space between rotor and magnet depicting a finer mesh compared to neighboring spaces.

It can be seen from Figure 4-5 that the density of mesh is very high at the air gap. This is essential since most of the electromagnetic interaction take place at the air gap. Triangular elements can also be more easily visualized in this figure

#### 4.3.4 Solution Scheme

Solutions for the Maxwell's equations are obtained by computing the geometry for a given angular position of the rotor and current in the coil. Since the geometry consist of 3 yokes, after every 120 degrees, the solution to the equations repeat. Hence the geometry is analyzed from 0 degree to 120 degree in steps of 2.5 degree. For a given angular position of the rotor, current in the terminal vary from 0 mA to 15 mA in steps of 3 mA.

Using the finite element method, a plot for torque against rotor position is obtained for various values of current in the coil. By integrating the curve over entire

cycle, a relationship between electromagnetic torque and current in the coil is established. This relationship together with one dimensional DC motor model is used describe a complete DC motor model.

#### **4.4 DC Motor Model**

The electromagnetic torque versus current plot obtained from the finite element analysis is used to develop a complete DC motor model by using experimental and physical parameters. Relationships for obtaining speed characteristics will be discussed in this section. To establish a complete model, constants like torque constant and induced electromotive force constants are needed to be calculated. Also, the finite element method did not consider the friction at the shaft. A suitable friction model will be also included in the DC motor model.

##### **4.4.1 Determination of Torque Constant**

The brush D.C. motor produces torque directly proportional to the power supplied to it. The core is located concentric to a set of permanent magnets. When current passes through the coils, a magnetic field is generated and this magnetic field interacts with external magnet field generated by the magnets. This interaction of the fields causes a torque to act on the rotor proportional to the current passing through the coils. The torque acting on the rotor is in effect caused by the Lorentz's force acting on the rotor [3] [4] [5]. Figure 4-1 illustrates the physics behind a D.C. motor taking just one turn in the consideration.

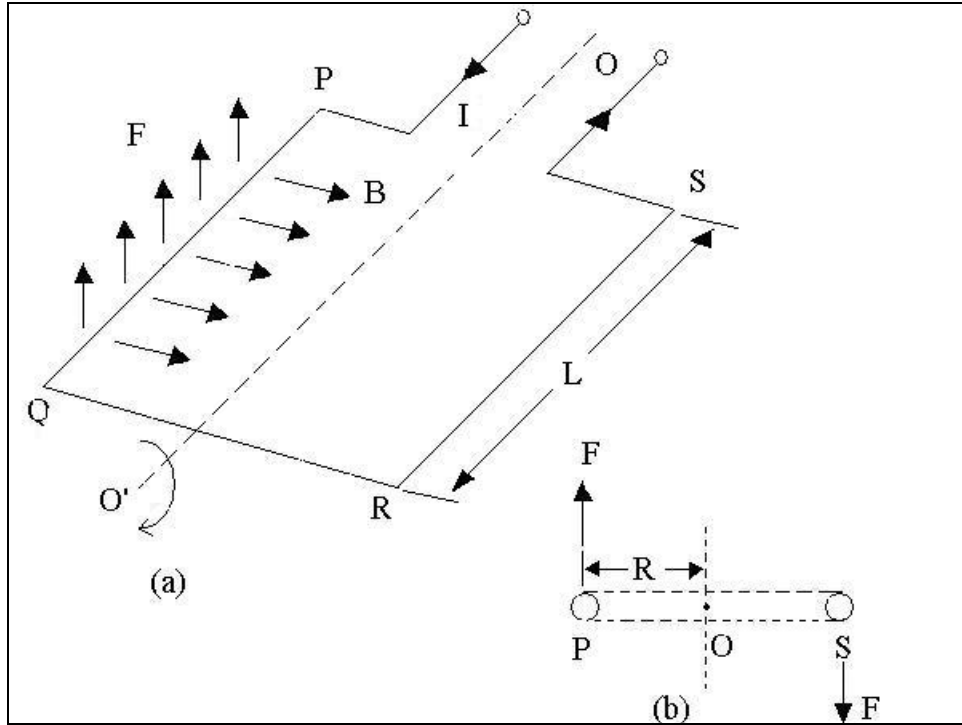


Figure 4-6. Schematic of D.C. Motor coil. A) Single current coil in an external magnetic field. B) Side view of the current carrying coil in external magnetic field.

The electromotive force  $F$  acting on a single coil is given by Lorentz force acting on a straight wire in external magnetic field.

$$F = IL \otimes B \quad (4.2)$$

where

$F$  = Force, Newton

$I$  = Current in coil, Ampere

$L$  = Length of conductor, Meter

$B$  = Magnetic field Intensity, Tesla

$\otimes$  = Cross product

Resolving the cross product,

$$F = ILB \times \sin\theta \quad (4.3)$$

where

$\theta$  = angle between vector along length L and magnetic field B.

Since both the vectors are always at right angle to each other  $\sin\theta = \sin 90 = 1$ .

Thus Equation (4.2) can be written as

$$F = ILB \quad (4.4)$$

Electromagnetic torque  $T_E$  acting on the rotor can be given by a product of the force F acting on the rotor and the radial distance R from the axis of rotation. Since force F acts on two lengths of the conductor, total force acting on the conductor is 2F. Thus electromagnetic torque is given by,

$$T_E = 2F \times R \quad (4.5)$$

Substituting Equation (4.4) in Equation (4.5),

$$T_E = 2RLBI \quad (4.6)$$

Thus for n number of turns, Torque acting can be calculated by simply multiplying Equation (4.6) by n.

$$T_E = 2nRLBI \quad (4.7)$$

Analytically, it is difficult to estimate B. To do so, high precision magnetic flux density meters are used. However, the magnitude of magnetic field intensity B remains constant since it is property of the permanent magnet. More convenient way of representing torque T is by expressing the multiple constant parameters collectively as a single constant. In case of motors, this constant is called motor constant or torque constant,  $K_T$ . This constant will be called torque constant hereafter in this report. Equation (4.7) is the representation of torque constant.

$$T_E = K_T \times I \quad (4.8)$$

#### 4.4.2 Determination of Voltage Constant

According to Faraday's Law, when a loop of current carrying coil is placed in a changing magnetic field, a voltage is induced in the coil. The voltage is called back electromotive force or back emf. The magnitude of back emf,  $V_{EMF}$  is given by Equation (4.10)

$$V_{EMF} = -\frac{d\phi}{dt} \quad (4.9)$$

where

$\phi$  = electromagnetic flux passing through the coil, Tesla. (meter)<sup>2</sup>

t = time, Second.

Flux  $\phi$  is expressed as magnetic field intensity B in a unit area A. Thus Equation (4.9) can be modified and written as

$$V_{EMF} = -\frac{d(BA)}{dt} \quad (4.10)$$

To simplify the model, it is assumed that magnetic field intensity is constant across the area under consideration. Since the size of magnets used is comparable to the size of the rotor, this assumption is fairly accurate. [3] [4] [5] [6]

Thus back emf Equation (4.10) can be written as

$$V_{EMF} = -B \frac{dA}{dt} \quad (4.11)$$

Figure 4-7 gives a schematic of a single coil on a rotor placed in permanent magnetic field.

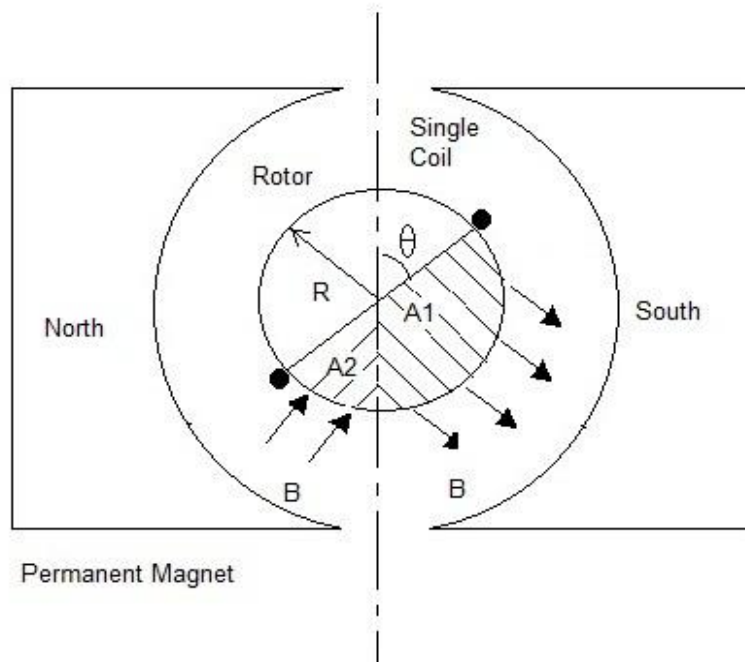


Figure 4-7. Schematic of a single coil rotating in an external magnetic field.

The area under the loop can be identified by areas A1 and A2. Assuming a sign convention that magnetic flux coming out of rotor is positive and flux going in the core is negative

The back emf equation can be thus written as

$$V_{EMF} = - \left[ B \frac{dA1}{dt} - B \frac{dA2}{dt} \right] \quad (4.12)$$

Thus combining the area terms, since B is a constant parameter,

$$V_{EMF} = -B \frac{d(A1 - A2)}{dt} \quad (4.13)$$

A1 and A2 can be expressed as

$$A1 = R \times (\pi - \theta) \times L \quad (4.14)$$

$$A2 = R \times \theta \times L \quad (4.15)$$

where,

R = radius of the rotor, meter

$\theta$  = angle traversed by arm of the rotor from the axis, Radian

L = Length of rotor measured in the plane of paper

Thus Equation (4.13) can be written as

$$V_{EMF} = -BRL \frac{d(\pi - 2\theta)}{dt} \quad (4.16)$$

Since  $\pi$  is a constant and  $\frac{d\theta}{dt} = \omega$  or angular velocity measured in radian/second,

Equation (4.16) is written as

$$V_{EMF} = 2BRL \times \omega \quad (4.17)$$

Generalizing the model for n turns,

$$V_{EMF} = 2nRLB \times \omega \quad (4.18)$$

The term  $2nRLB$  is collectively called back emf constant  $K_{EMF}$ .

Thus back emf generated is given by Equation (4.19) in terms of back emf constant and rotational speed,

$$V_{EMF} = K_{EMF} \times \omega \quad (4.19)$$

In an ideal motor,  $K_T = K_{EMF} = 2nRLB$  when expressed in a consistent unit system.

However, in actual motors, values of  $K_T$  and  $K_{EMF}$  are not equal, since there always exists a stray magnetic field

### 4.4.3 Motor Speed Calculation

Figure 4-8 shows an equivalent circuit model of a D.C. motor. Since all the experimental results are achieved at steady state, only a steady state model is constructed. Hence the equivalent D.C. motor circuit does not include inductance.

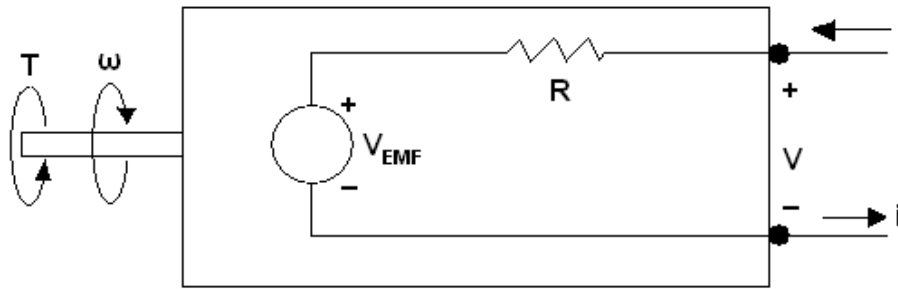


Figure 4-8. Equivalent Circuit for a D.C. electric motor [7].

Voltage across the terminal can be expressed as

$$V = V_{EMF} + IR \quad (4.20)$$

When no resisting torque is applied, the current passing through the motor is  $I_{Free}$  and the speed of rotation is  $\omega_{Free}$ . The equation for back emf constant is thus given by combining Equation (4.19) and Equation (4.20) and eliminating  $V_{EMF}$  [8]

$$K_{EMF} = \frac{V - IR}{\omega} \quad (4.20)$$

From Equation (4.9),

$$K_T = \frac{T}{I} \quad (4.21)$$

### 4.4.4 Parameterization of Voltage Constant

Parameterization of constant implies that it is expressed as a factor of other constant that can be either measured directly or can be calculated from the governing

equations. In this case, the voltage constant  $K_{EMF}$  is expressed as a factor of the factor

$\frac{K_T}{K_{EMF}}$  is defined as  $\gamma$ . Using the parameterization factor  $\gamma$  and taking a ratio of

Equation (4.21) and Equation (4.20),

$$\gamma = \frac{T \times \omega}{I \times (V - IR)} \quad (4.22)$$

Re arranging the terms in Equation 4.22 can be thus expressed as

$$T = [\gamma \times I \times (V - IR)] \times \frac{1}{\omega} \quad (4.23)$$

Equation (4.23) gives a model for electromagnetic torque as a function of motor speed when energized by a voltage  $V$ . However, this model over predicts the torque since it does not include the effects with friction. Friction model is discussed in the following section.

#### 4.4.5 Friction Model

Several friction models have been discussed extensively in literature. Models for friction compensation are proposed by Walrath [9] and Dahl [10]. Model proposed by Walrath does not consider the dynamic component of friction while the model proposed by Dahl does not account for static friction. A friction model used in this study was proposed by Canudas et al. [11] and includes both static (coulomb) friction and dynamic (viscous) friction. The model is given by,

$$T_F = (\alpha \times \omega) + \beta \quad (4.24)$$

Using the experimental data, constants  $\alpha$  and  $\beta$  can be determined. The actual friction model used is given by

$$T_F = 5.992E-04 \times \omega - 0.5715 \quad (4.25)$$

The load motor torque  $T_L$  can be thus expressed as,

$$T_L = T_E - T_F \quad (4.26)$$

By using curve fit equations for speed and torque, free speed,  $\omega_{Free}$  and stalling torque  $T_{Stall}$  can be calculated. Stalling can be calculated by knowing the value of motor terminal resistance R and actuation voltage V.

$$I_{stall} = \frac{V}{R} \quad (4.27)$$

Thus current consumed by motor when no resisting torque is acting on the motor can be calculated using

$$\frac{1}{\gamma} \left( \frac{\tau_{stall}}{I_{Stall} - I_{Free}} \right) = \left( \frac{V - I_{Free}R}{\omega_{Free}} \right) \quad (4.28)$$

Equation (4.26) can be used to plot the load torque and the motor speed curve.

Efficiency  $\eta$  of a DC Motor is given by,

$$\eta = \frac{T_L \times \omega}{V \times I} \quad (4.29)$$

#### 4.4.6 FEM and DC Motor Model Results

In the next chapter, results of the finite element analysis are discussed. The results obtained from this analysis are used to construct a steady state motor model as discussed earlier in this chapter. These results will be then compared to the experimental results.

## CHAPTER 5 MODELING RESULTS

In previous chapters, experimental data for DC motor was discussed. In last chapter it was discussed that an open source finite element analysis tool, FEMM can be used to solve Maxwell's partial differential equations which govern the interaction between current and charges and the electromagnetic field. The motor geometry was discretized in triangular elements. A steady state DC motor model was also discussed. Finally a linear friction model was discussed. The solutions are explained in detail in this section. The torque current relation obtained from finite element method will be then used with the DC motor model and friction model to obtain motor characteristic curves.

### **5.1 FEM Results**

The FEMM code was used to solve the motor geometry described in Figure 4-1 and the result shown in Figure 5-1 is a magnetic flux density plot with the rotor being at reference position. As explained in Figure 4-2, the commutator divides the current between coil 2 and coil3. Since the resistance of both the coils is equal, the current gets divided equally. Hence a current of 0.1 mA in flows through coil 1 and current of 0.05 mA flows through coil 2 and coil 3. Figure 5-2 Magnetic field intensities with flux lines superimposed at the reference orientation

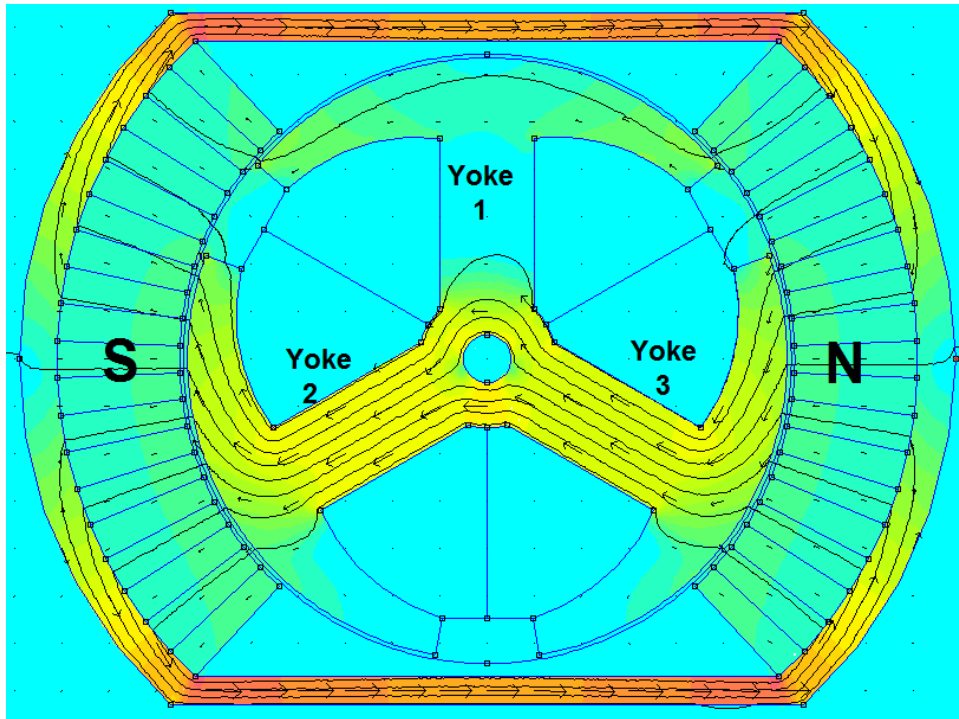


Figure 5-1. Magnetic flux densities at the reference position.

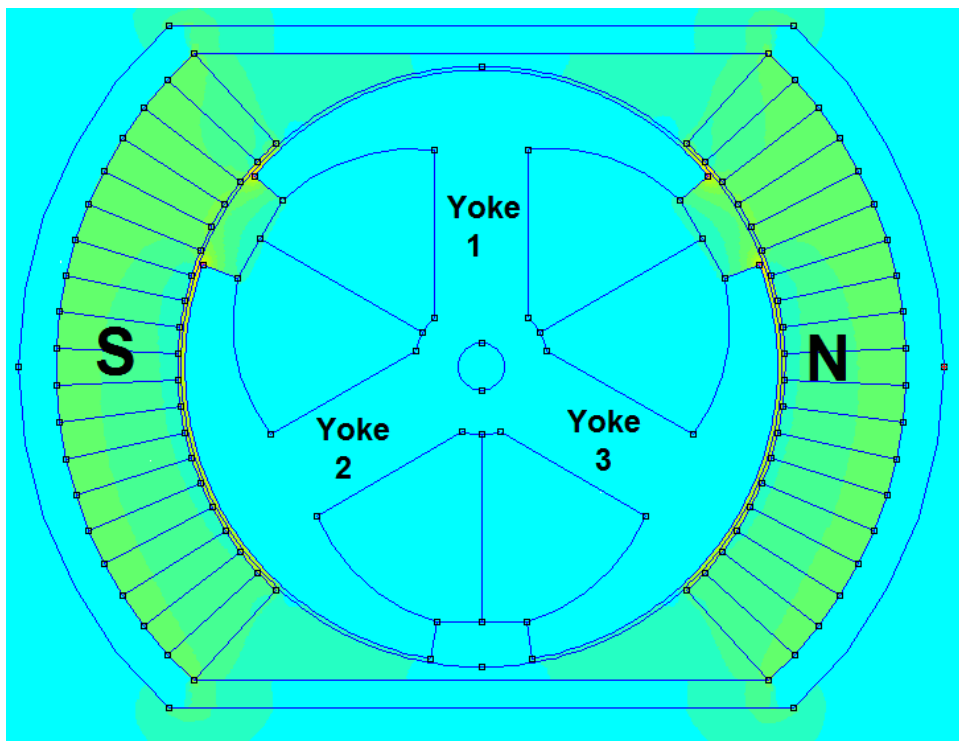


Figure 5-2. Magnetic field intensities at the reference position.

It can be seen in Figure 5-1 that flux lines enter Yoke 3 and leave Yoke 2. The magnetic flux lines follow the north south direction passing through the electromagnetic field generated by rotor. In the rotor, the flux density is highest at the Yoke 2 and Yoke 3. This indicates that torque induced on these parts of rotor is more than any other on the rotor. The direction of force induced on the rotor is given by Fleming's left hand rule. Thus torque is induced on the rotor. Figure 5-2 shows the magnetic field intensities. The field intensities are high at the air gap, particularly between the magnet and the rotor. A closer look at the air gap can be seen in Figure 5-3

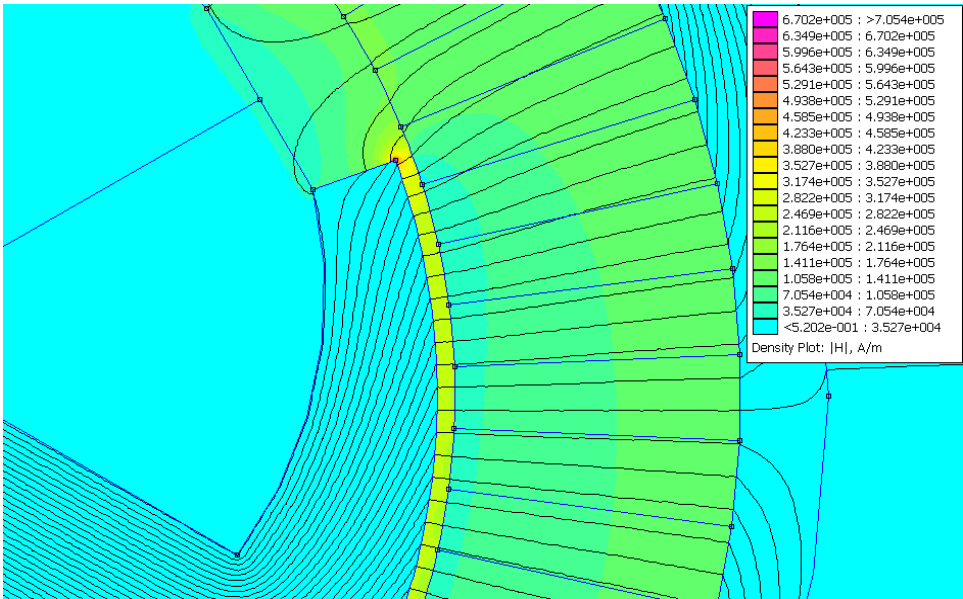


Figure 5-3. Magnetic field intensity at the air gap between magnet and rotor. The magnetic field intensities are highest at the air gap because this region serves as the area where magnetic fields generated by electromagnet and permanent magnet interact. The vector product of both the fields results in higher magnetic intensity.

The solution scheme explained in previous chapter was applied to the finite element model. A series of simulation as explained in that section was carried out and

the values of torque obtained for each simulation are plotted in Figure 5-4. Figure 5-4 shows a plot of variation of instantaneous torque as a function of rotor angular position.

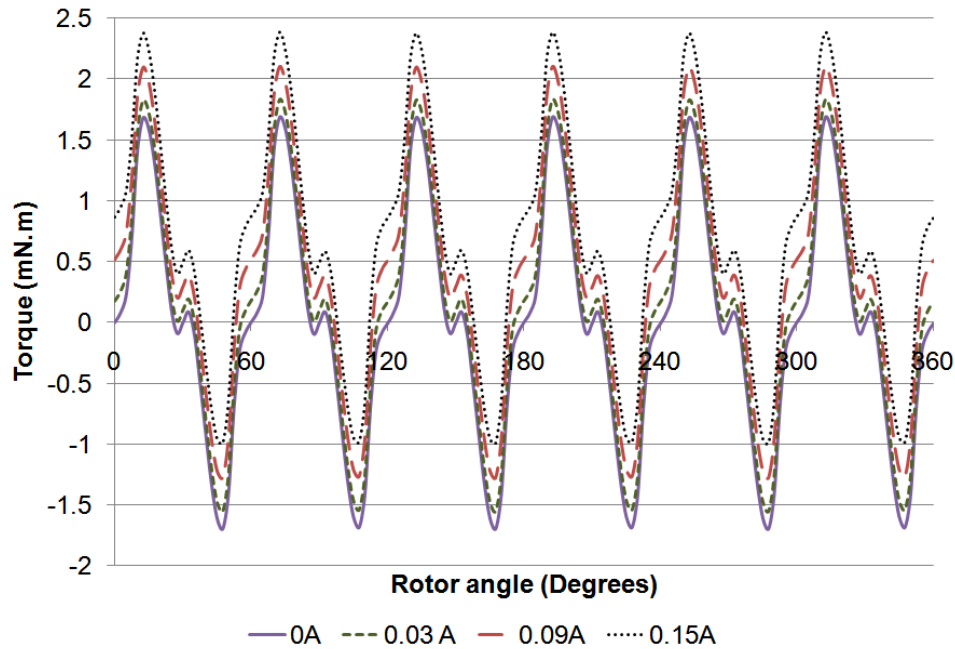


Figure 5-4. Variation of torque with rotor angular position.

In Figure 5-4, six positive spikes and six negative spikes can be seen. Six spikes are the result of three rotor yokes rotating past two permanent magnets. Positive spikes in torque are caused by the electromagnet being attracted by the permanent magnet thus assisting the rotation. Momentary negative spikes are observed when the electromagnets are repelled by the permanent magnets. Since the magnitude and the duration torque being in positive region is more than it is in negative region, a net positive torque is experienced on the rotor. The value of torque generated at the shaft for a given current as a function of the position of the rotor, as shown in Figure 5-4 is integrated over the entire cycle using MATLAB's shape preserving curve fit. The averaged torque over the entire cycle,  $T_{Avg}$ , is then given by,

$$T_{Avg} = \frac{1}{2\pi} \int_0^{2\pi} T(\theta) d\theta \quad (5.1)$$

Figure 5-5 shows a plot of  $T_{Avg}$  against current. The results presented in this plot are compared with the experimental results described earlier in Chapter 3.

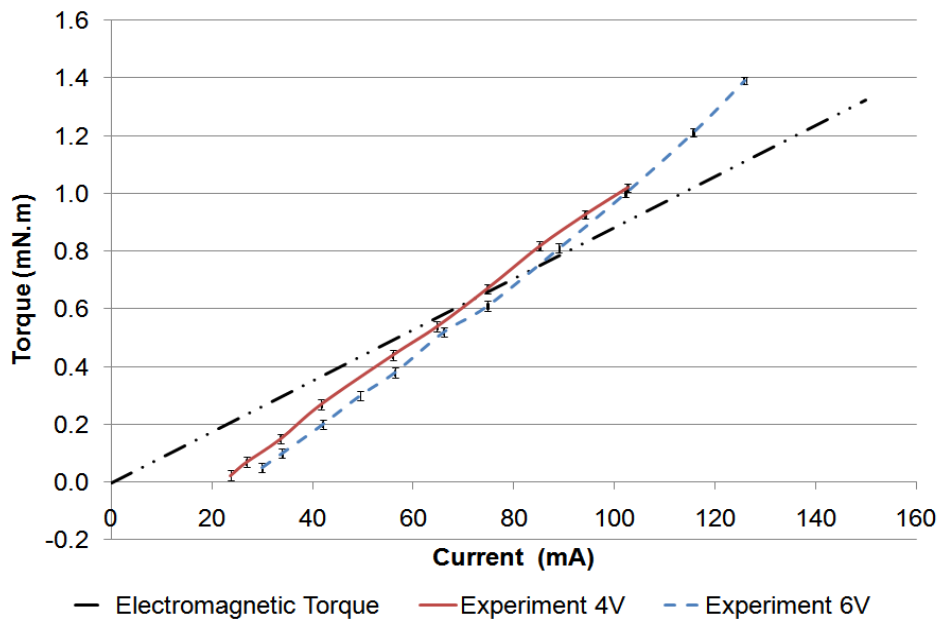


Figure 5-5. Plot for electromagnetic torque and experimental torque versus current. The x intercept for the experimental values shown in Figure 5-5 are the free current or the current consumed by motor when no resisting torque is applied. The electromagnetic torque, however, does not have this x intercept because the electromagnetic torque is the torque generated at the shaft while the experimental torque is the resisting torque on the motor. For zero current passing through the coils, no electromagnetic torque is generated. The torque increases linearly with current in the coil and this phenomenon is also explained by Equation (4.8).

## 5.2 Application of DC Motor Model to FEM Results

A DC motor model was discussed in Chapter 4. Figure 5-6 shows a plot of torque versus speed for experimental and FEM results as given by Equation 4.26. The model was evaluated at the energizing voltages of 4V and 6V.

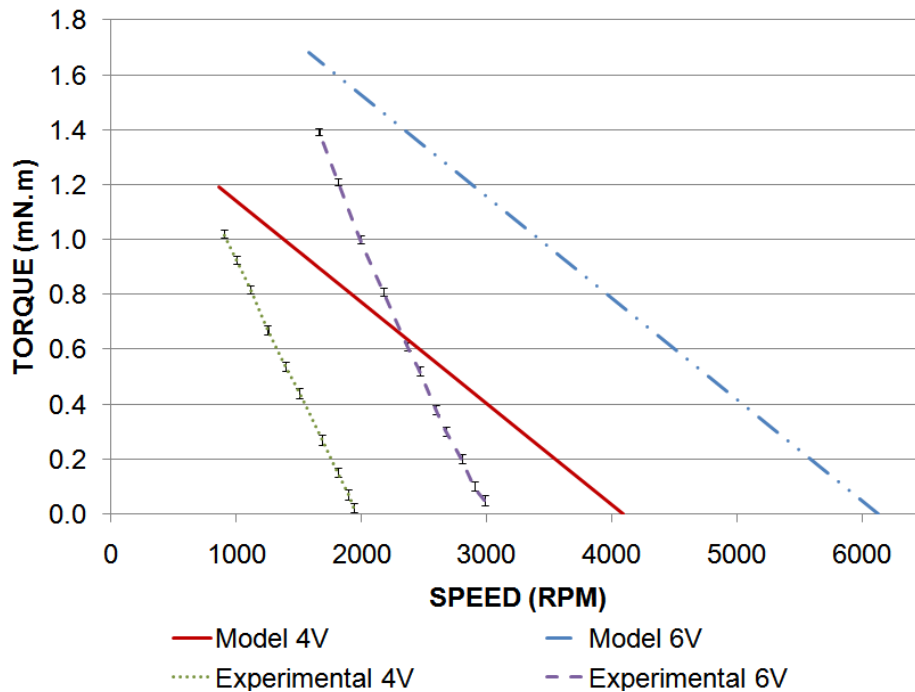


Figure 5-6. Comparison of experimental and analytical electromagnetic torque values for 4V and 6V

In the Figure 5-6, the model considers only the electromagnetic torque. It can be seen from the plot that the slope of the electromagnetic torque is much lesser than the experimental results. This can be seen for both the cases of actuation voltages. Free speed for electromagnetic torque in case of actuation voltage of 4V is about 4000 rpm, whereas in actual experiments, free speed recorded was about 2000 rpm. The difference in the speed increases linearly as the resisting torque drops. The reason for high rotation speed for electromagnetic torque is because it does not take into

consideration the friction. Figure 5-7 shows a plot of load torque when friction model described in previous chapter is taken into account.

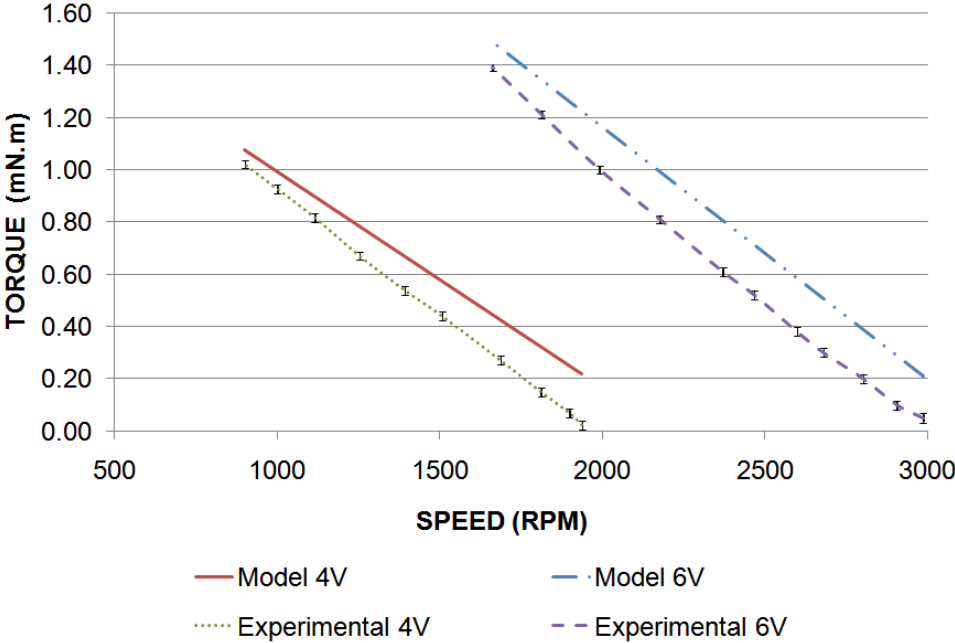


Figure 5-7. Comparison of experimental and analytical load torque values for 4V and 6V

From Figure 5-7 it can be seen that the model agrees with experimental results fairly well at lower speeds. However, the disagreement increases as the motor speed increases. The variation in the experimental and analytical values increases exponentially with the increase in the speed. Using Equation (4.31), efficiency can be calculated and Figure 5-8 shows a plot of analytical and experimental values of efficiency as a function of motor speed.

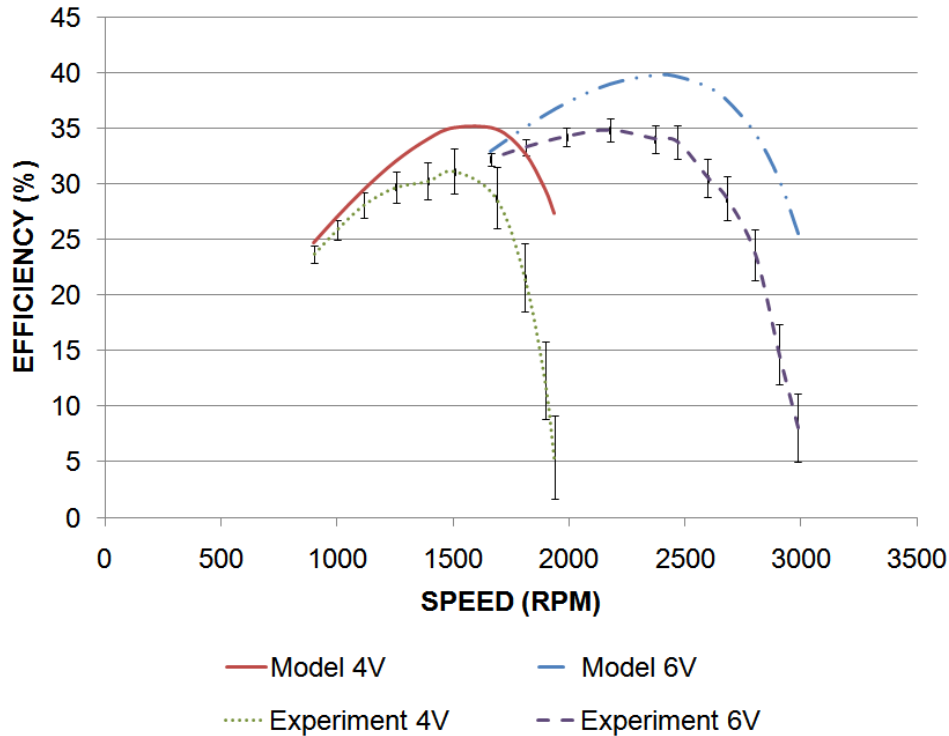


Figure 5-8. Comparison of experimental and analytical motor efficiency for 4V and 6V. From Figure 5-7 and Figure 5-8 it can be seen that the model predicts higher torque at higher rpm. And Equation (4.31) shows that for higher torque, the efficiency is also higher for same speed and input power. The efficiency predicted by the model is thus higher than the experimental values.

This chapter discussed that by employing a magnetostatic finite element code, solutions for magnetic flux densities, magnetic field intensities and torque acting on current carrying conductors can be obtained. By using a steady state motor model and a linear friction model, an analytical map of DC motor performance can be obtained. The results obtained from the model were compared with the experimental values. By applying appropriate curve fit equations, analytical values for stalling torque and free speed, stalling current and free current can be obtained. Table 5-1 shows a comparison of experimental and analytical values of these parameters.

Table 5-1. Comparison of experimental and analytical values of motor parameters

	4V		6V	
	Experiment	Model	Experiment	Model
$T_{Stall}$ (mN.m)	1.88	1.82	3.04	3.10
$\omega_{Free}$ (RPM)	1966	2201	2993	3202
$I_{Stall}$ (mA)	170	162	250	243
$I_{Free}$ (mA)	21.5	22.2	27.8	28.1

## CHAPTER 6 CONCLUSIONS AND RECOMMENDATIONS FOR FUTURE WORK

In this work, apparatus were built for testing micro pumps and DC motors. Characteristic curves for positive displacement micro pump and permanent magnet brush type DC motor were achieved with good repeatability. Uncertainty analysis was performed on the data obtained from these apparatus. Using the results from both the apparatus, experimental results for the pump's hydrodynamic performance were inferred. The results obtained from these apparatus provide a good validation step for all future fluid dynamics modeling efforts. A steady state model for permanent magnet brush type DC motor was also introduced. The DC motor models discussed in the literature depend on manufacturer's data to construct a model. In this study, a finite element analysis was done using an open source package, FEMM, to calculate the electromagnetic parameters for DC motor such as magnetic field density and magnetic field intensity. The code has a capability to calculate torque produced by the motor as functions of coil current, rotor position and material properties. By employing modeling techniques discussed by several authors, motor characteristic curves such as torque and efficiency as functions of motor speed and energizing voltage were constructed. A friction model, which accounted for coulomb and viscous friction, was also added to the electromagnetic model to approximate the actual DC motor under consideration. The results obtained from this model were presented as a comparison with the experimentation results.

It was seen that the analytical and experimental values of torque and efficiency as a function of speed matched closely at low speeds. However, at higher speeds, the difference between these results increased sharply. One of the possible reasons for this

inconsistency can be the incomprehensive friction model. The friction model introduced in this work accounted for shaft friction. However, friction at brush commutator interface was not taken into consideration. Also, wear on the graphite brushes and its contribution to the friction was not taken into consideration.

The experimental techniques presented in this have allowed pump testing with flow rates up to 150 ml/min and back pressure up to 25 psi, and DC motor testing with power consumption up to 4W. The modeling techniques presented in this work allow a motor designer to vary the motor component dimensions and material properties to obtain approximate characteristic curves for design purposes. This model in conjunction with a fluid dynamics model will form a complete micro pump model.

The main objective of this research was to support DMFC development activities. By employing the micro pump model, a fairly accurate estimate of parasitic power consumption can be achieved. Since the pump characteristic curves can be achieved analytically, the results can be used to create a pump performance map. This will assist a fuel cell control engineer to estimate flow rate and power consumption for recirculation pump as a function of external load. Some of the observations from the experimental results were

- The effect of head on pump power consumption was very small.
- Pump energizing voltage does not have any effect on pump efficiency till the head is 10 psi. If head more than 10 psi is acting, the pump is more efficient when operated at 6V.
- The hydrodynamic efficiency is nearly insensitive to pump energizing voltage.

- For a given amount of current flowing through the coils, only a certain constant amount of torque will be generated. The energizing voltage dictates the speed at which this torque is available.

In future, physical phenomena that caused mismatch of analytical and experimental results at higher motor speeds can be investigated. Only the bearing friction has been taken into consideration. However, friction also exists at the interface of brush and commutator. Experiments conducted on brush type motor have indicated the degradation of motor performance with time. The degradation of the brushes and the rate at which degradation occurs can be analyzed analytically. The finite element model presented in this study assumes all materials to be homogenous. A more comprehensive model will also take into account the non homogeneity of these materials. The FEM tool, FEMM, is a steady state two dimensional analysis tool. Advanced FEM tools like ANSYS can be employed to get dynamic, three dimensional results.

APPENDIX 1  
UNCERTAINTY ANALYSIS

**1.1 UF Pump Test Apparatus**

**1.1.1 Energizing Voltage for pump-motor combination**

Accuracy of the voltage input module is 0.07% of the reading [1]. Thus uncertainty in measuring Voltage  $W(V)$  is given by

$$W(V) = \frac{0.07}{100} \times V \quad (A1.1)$$

**1.1.2 Current**

The voltage across the shunt is measured by the voltage input module [1]. Thus uncertainty in current measurement  $W(I)$  is given by

$$W(I) = \frac{0.07}{100} \times V \quad (A1.2)$$

**1.1.3 Flow rate**

The Rotameter used in the setup is an Omega Rotameter with an accuracy of  $\pm 2\%$  of full scale deflection. The full scale reading on flow meter is 150 ml/min. Thus the uncertainty in flow rate measurement,  $W(Q)$ , ml/min

$$W(Q) = 3 \quad (A1.3)$$

**1.1.4 Differential Pressure**

Since the differential pressure is a function of current, uncertainty in the measured pressure is a function of current and the accuracy with which the current is measured by the data acquisition hardware. Uncertainty in measuring differential pressure  $W(\Delta P)$ , psi is given by,

For 0-5 psi gauge:

$$W(\Delta P) = 0.3206 \times W(I) \times I \quad (A1.4)$$

For 0-25 psi gauge:

$$W(\Delta P) = 1.5802 \times W(I) \times I \quad (A1.5)$$

### 1.1.5 Input Power

Uncertainty in the Input Power  $W(P_{IN})$ , Watt is given by

$$W(P_{IN}) = \left[ (V \times W(I))^2 + (I \times W(V))^2 \right]^{1/2} \quad (A1.6)$$

### 1.1.6 Output Power

Uncertainty in Output Power  $W(P_{OUT})$ , Watt is given by

$$W(P_{OUT}) = \left[ \left( (\Delta P \times 6894.757) \times \left( \frac{W(Q) \times 10^{-6}}{60} \right) \right)^2 + \left( (W(\Delta P) \times 6894.757) \times \left( \frac{Q \times 10^{-6}}{60} \right) \right)^2 \right]^{1/2} \quad (A1.7)$$

### 1.1.7 Efficiency

Uncertainty in efficiency  $W(\eta)$  is given by

$$W(\eta) = \left[ \left( \frac{W(P_{OUT})}{P_{IN}} \right)^2 + \left( \frac{P_{OUT} \times W(P_{IN})}{P_{IN}^2} \right)^2 \right]^{1/2} \times 100 \quad (A1.8)$$

## 1.2 Micro-dynamometer

### 1.2.1 Voltage

Accuracy of the voltage input module is 0.2% of the reading. Thus uncertainty in measuring Voltage  $W(V)$  is given by

$$W(V) = \frac{0.2}{100} \times V \quad (A1.9)$$

### 1.2.2 Current

Current is measured using a precision shunt resistor. The voltage across the shunt is measured by the voltage input module. Thus uncertainty in current measurement  $W(I)$  is given by

$$W(I) = \frac{0.2}{100} \times I \quad (\text{A1.10})$$

### 1.2.3 Angle of deflection

The accuracy of rotary encoder is  $\pm 0.5^0$  Deg or  $\pm 0.00873$  radians.

Hence the uncertainty in measuring angle,  $W(\theta)$  in radians is

$$W(\theta) = \pm 0.00873 \quad (\text{A1.11})$$

### 1.2.4 Torque

Uncertainty in Torque  $\tau$ ,  $W(\tau)$  in N-m is given by,

$$W(\tau) = g \times \frac{l}{2} \times \cos(\theta) \times (m_{CW} - m_{Mag}) \times W(\theta) \quad (\text{A1.12})$$

### 1.2.5 Motor speed

Accuracy of optical tachometer as specified by manufacturer is  $\pm 0.05\%$  of the reading.

Thus the uncertainty in measuring motor speed  $W(\omega)$  in RPM is

$$W(\omega) = \frac{0.05}{100} \times \omega \quad (\text{A1.13})$$

### 1.2.6 Input power

Uncertainty in the Input Power,  $W(P_{IN})$  Watt is given by

$$W(P_{IN}) = \left[ (V \times W(I))^2 + (I \times W(V))^2 \right]^{1/2} \quad (\text{A1.14})$$

### 1.2.7 Output power

Uncertainty in measuring output power  $W(P_{OUT})$  in Watts is given by

$$W(P_{OUT}) = \left[ (\tau \times W(\omega))^2 + (\omega \times W(\tau))^2 \right]^{1/2} \quad (\text{A1.15})$$

### 1.2.8 Efficiency

Uncertainty in efficiency  $W(\eta)$  is given by

$$W(\eta) = \left[ \left( \frac{W(P_{OUT})}{P_{IN}} \right)^2 + \left( \frac{P_{OUT} \times W(P_{IN})}{P_{IN}^2} \right)^2 \right]^{1/2} \times 100 \quad (\text{A1.16})$$

## 1.3 Inferred Results

### 1.3.1 Pump Efficiency

Uncertainty associated with calculating pump efficiency  $W(\eta_{pump})$  is given by

$$W(\eta_{pump}) = \left[ \left( \frac{W(\eta_{overall})}{\eta_{motor}} \right)^2 + \left( \frac{\eta_{overall} \times W(\eta_{motor})}{\eta_{motor}} \right)^2 \right]^{1/2} \quad (\text{A1.17})$$

APPENDIX 2  
MODEL GEOMETRY

2.1 Motor Rotor

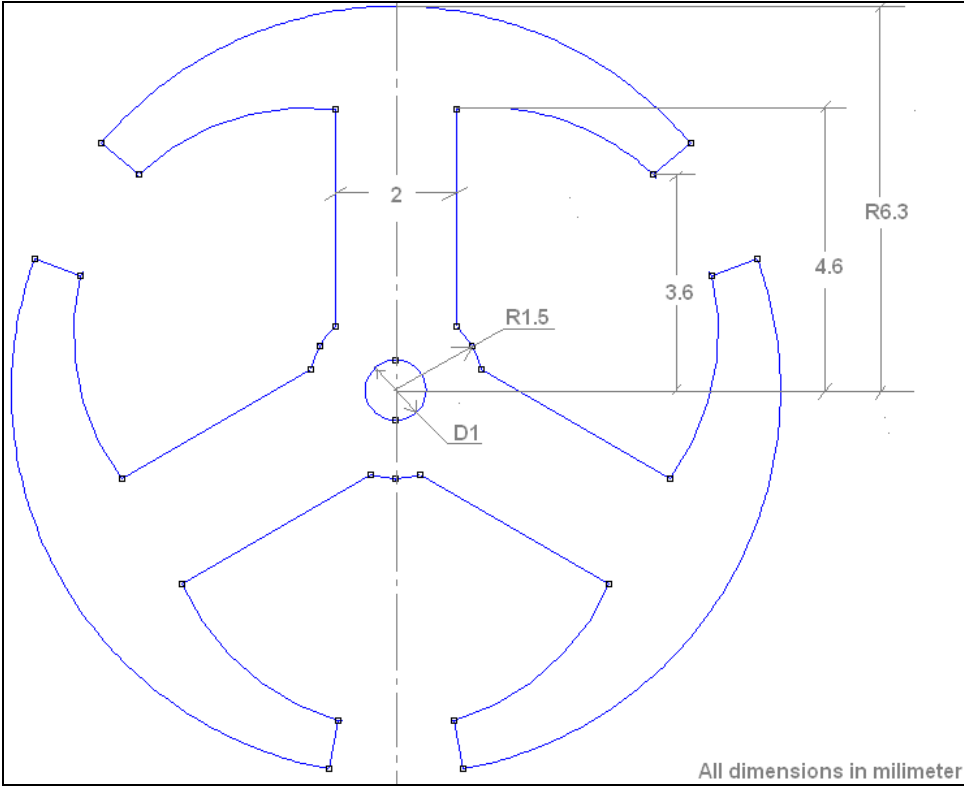


Figure Appendix 2-1. Laminated steel rotor in the DC Motor

## 2.2 Motor Casing

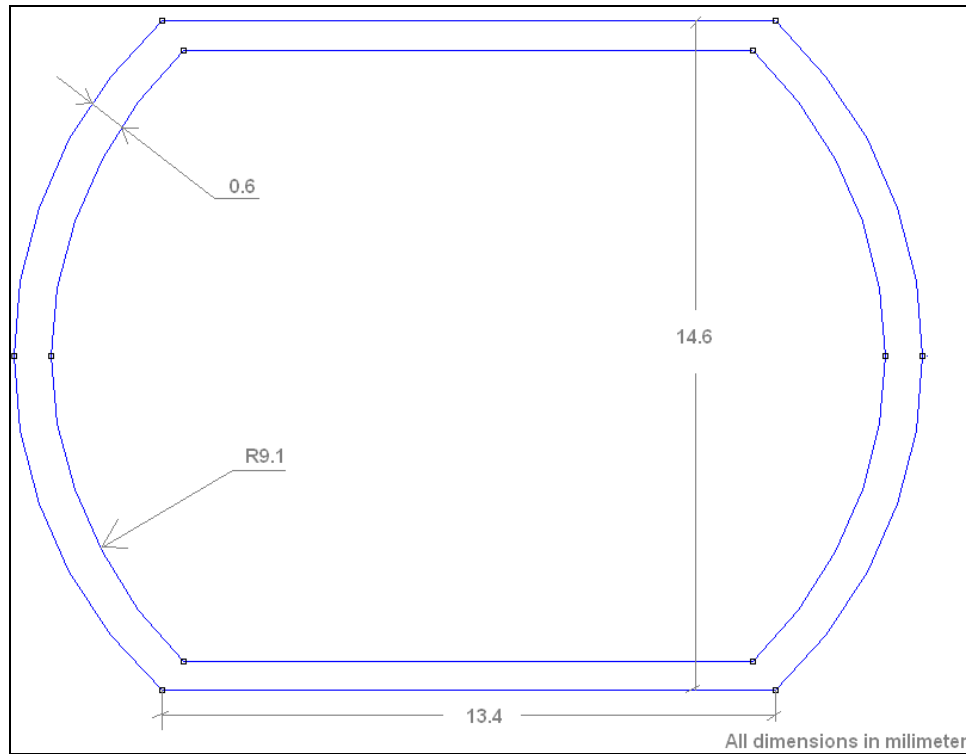


Figure Appendix 2-2. Steel casing in the DC motor

### 2.3 Permanent Magnet

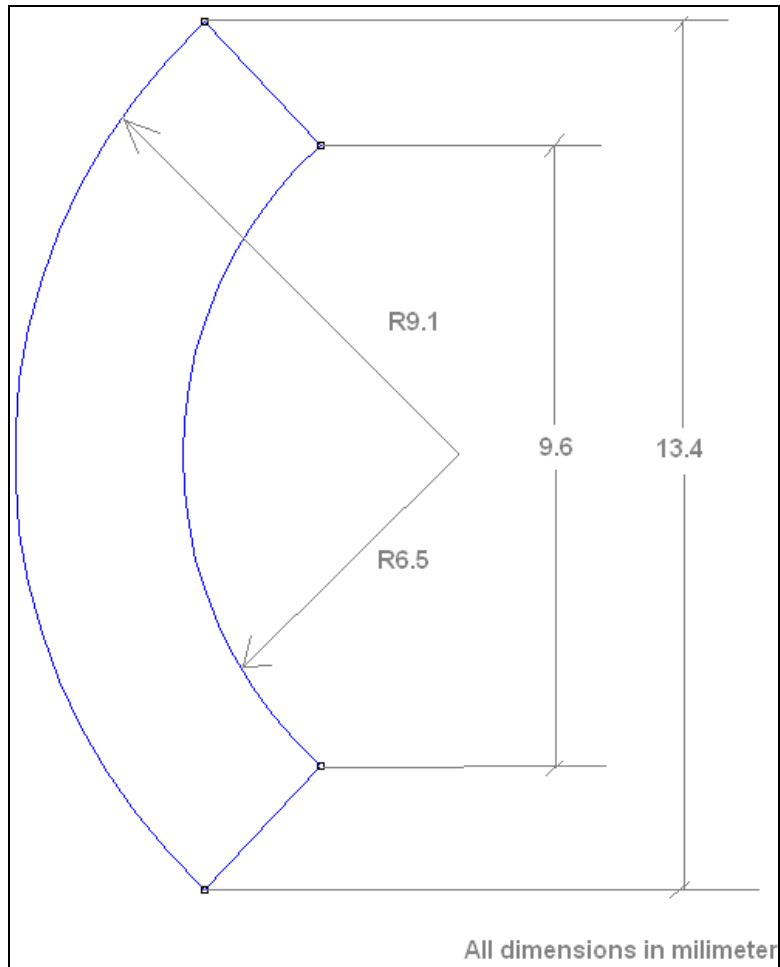


Figure Appendix 2-3. Ceramic magnet in the DC motor

## LIST OF REFERENCES

1. University of North Florida, Micro dynamometer Project Report, Internal document.
2. D. C. Meeker, Finite Element Method Magnetics, Version 4.0.1 (03Dec2006 Build), <http://www.femm.info>
3. Chapman, S.J. Electric Machinery Fundamentals, McGraw-Hill, New York, 1991
4. Chiasson, J. The Physics of DC Motor for Control Courses, Notes. University of Pittsburgh, PA
5. Matsch, L. Electromagnetic and Electromechanical Machines. Harper and Row, New York, 1977.
6. Nise, N. Control Systems Engineering, Appendix-H. Wiley and sons, 2008
7. Mark D. First order DC electric motor model, MIT Aero & Astro, February 2007
8. Heinzmann, K. Mikus, K. Introduction to Motors, 2005.  
<https://research.cc.gatech.edu/humanoids/sites/edu.humanoids/files/IntroToMotors.pdf>
9. Walrath, C.D. "Adaptive Bearing Friction Compensation Based on Recent Knowledge of Dynamic Friction". Automatica. Vol. 20. No. 6, pp. 717-727, 1984.
10. Dahl, P.R. "Measurement of Solid Friction Parameters of Ball Bearings". Proceeding of 6th Annual Symposium on Incremental Motion Control Systems and Devices, University of Illinois, 1977.
11. Canudas, C. Astrom, K.J. and Braun, K. Adaptive Friction compensation in DC Motor Drives, IEEE International Conference on Robotics and Automation, 1986.

## BIOGRAPHICAL SKETCH

Anupam Patil was born in Mumbai, India, in 1985 and was raised by a surgeon father and a banker mother in a scenic coastal town of Alibag, India. Anupam completed his Bachelor of Engineering in mechanical engineering from Veermata Jijabai Technological Institute, Mumbai in 2007. After graduation, Anupam worked as a Product Development Engineer at the Automotive Sector of Mahindra and Mahindra where his work focused on vehicle performance and vehicle dynamics modeling.

Anupam enrolled for the Masters of Science program in mechanical engineering at University of Florida in August 2008 under guidance of Dr. William Lear, Dr. James Fletcher and Dr. Oscar Crisalle. During his Masters program, he served as a Research Assistant at the Fuel Cell Research Laboratory. Anupam received his Master of Science in mechanical engineering in August 2011. Upon completion of his degree, He started working fulltime for Cummins, Inc as a Fuel Systems Performance Engineer. Anupam intends to continue to contribute to the field of clean energy.